AGU PUBLICATIONS

Geochemistry, Geophysics, Geosystems

RESEARCH ARTICLE
10.1002/2017GC007112

Evaluating the Influence of Plate Boundary Friction and Mantle Viscosity on Plate Velocities

A. Osei Tutu[1,2], S. V. Sobolev[1,2], B. Steinberger[1,3], A. A. Popov[4], and I. Rogozhina[1,5]

[1]GFZ German Research Centre for Geosciences, Potsdam, Germany, [2]Institute of Earth and Environmental Science, University of Potsdam, Potsdam, Germany, [3]Centre for Earth Evolution and Dynamics, University of Oslo, Oslo, Norway, [4]Institute of Geosciences, Johann Gutenberg University, Mainz, Germany, [5]Marum Centre for Marine Environmental Sciences, University of Bremen, Bremen, Germany

Key Points:
- We model plate motions using a global model that combines a 3-D visco-elasto-plastic rheology in the upper 300 km and a radial viscosity structure in the mantle
- We estimate interplate friction and upper mantle viscosity to reproduce observed plate velocities as well as the magnitude and location of the Euler pole of lithosphere net rotation
- Key parameters required to fit observations are a friction coefficient of less than 0.05 at plate boundaries and a minimum mantle viscosity cut-off of 1–5 $\cdot 10^{19}$ Pas

Supporting Information:
- Supporting Information S1
- Data Set S1
- Data Set S2
- Data Set S3
- Data Set S4
- Data Set S5
- Data Set S6
- Data Set S7
- Data Set S8
- Data Set S9
- Data Set S10

Correspondence to:
A. Osei Tutu,
oseitutu@gfz-potsdam.de

Citation:
Osei Tutu, A., Sobolev, S. V., Steinberger, B., Popov, A. A., & Rogozhina, I. (2018). Evaluating the influence of plate boundary friction and mantle viscosity on plate velocities. *Geochemistry, Geophysics, Geosystems*, *19*, 642–666. https://doi.org/10.1002/2017GC007112

Received 7 JUL 2017
Accepted 11 JAN 2018
Accepted article online 1 FEB 2018
Published online 10 MAR 2018

Abstract Lithospheric plates move over the low-viscosity asthenosphere balancing several forces, which generate plate motions. We use a global 3-D lithosphere-asthenosphere model (SLIM3D) with visco-elasto-plastic rheology coupled to a spectral model of mantle flow at 300 km depth to quantify the influence of intra-plate friction and asthenospheric viscosity on plate velocities. We account for the brittle-ductile deformation at plate boundaries (yield stress) using a plate boundary friction coefficient to predict the present-day plate motion and net rotation of the lithospheric plates. Previous modeling studies have suggested that small friction coefficients ($\mu < 0.1$, yield stress ~ 100 MPa) can lead to plate tectonics in models of mantle convection. Here we show that in order to match the observed present-day plate motion and net rotation, the frictional parameter must be less than 0.05. We obtain a good fit with the magnitude and orientation of the observed plate velocities (NUVEL-1A) in a no-net-rotation (NNR) reference frame with $\mu < 0.05$ and a minimum asthenosphere viscosity of $\sim 5 \cdot 10^{19}$ Pas to 10^{20} Pas. Our estimates of net rotation (NR) of the lithosphere suggest that amplitudes $\sim 0.1-0.2$ (°/Ma), similar to most observation-based estimates, can be obtained with asthenosphere viscosity cutoff values of $\sim 10^{19}$ Pas to $5 \cdot 10^{19}$ Pas and friction coefficients $\mu < 0.05$.

1. Introduction

Compared to the other planets in our solar system the uniqueness of the Earth is related to the presence of plate tectonics, which is also believed to have influenced the development of the only known habitable environment (Nesbitt & Young, 1982; Raymo & Ruddiman, 1992; Veevers, 1990). This fact has enhanced a general interest in the concept of plate tectonics and has made it a focus of numerous studies in the past few decades. For example, Davies (1978) showed that the force balance contribution due to whole-mantle convection is non-negligible compared to other driving and resistive forces acting on the lithospheric plates. The total net torque on the lithosphere plates from plate boundary forces should be balanced by the basal shear stresses from the mantle beneath (Hager & O'Connell, 1981; Turcotte & Oxburgh, 1967). The stress that builds up in the crust and lithosphere (Bird, 1989; Bird et al., 2008; Zoback, 1992, Zoback et al., 1989) is shown to originate from both shallow and deep sources, with a larger part of these stresses coming from subducting plates (Forsyth & Uyeda, 1975). Previous studies have enabled a relatively good understanding of the factors that cause plate motion over a low-viscosity asthenosphere. Through geological observations (DeMets et al., 2010), combined with spectral (Conrad & Lithgow-Bertelloni, 2002; Hager & O'Connell, 1981) and finite element/finite difference numerical approaches (Conrad & Lithgow-Bertelloni, 2002; Minster et al., 1974; Moresi et al., 2000; Zhong & Gurnis, 1995), the knowledge about some of the major contributing factors was developed. Among such factors are the basal driving force acting on the lithosphere due to mantle convection (i.e. internal buoyancy force), plate boundary forces such as slab pull, ridge push, inter-plate friction and trench resistance, and the cratonic root resistance. Each of these forces is either a driving or a resisting force contributing to the total force balance of global plate motions. While one branch of studies has used kinematic analysis to quantify individual forces (Becker & O'Connell, 2001; Becker et al., 2015; Davies, 1978; Hager & O'Connell, 1979; Lithgow-Bertelloni & Richards, 1998; Torsvik et al., 2010) that come into play for the plates to move, other studies (Alisic et al., 2012; Becker, 2006; Lithgow-

Bertelloni & Richards, 1995; Schellart, 2004; Stadler et al., 2010) have sought to explain rheological implications of the moving plates for both the upper and lower mantle. Nonetheless, studies that have tried to identify and quantify these individual driving and resisting forces have also arrived at non-unique conclusions regarding some force contributions. For example, Lithgow-Bertelloni and Richards (1998) suggested that subducting slabs acting at the margin of a moving plate at shallow depths together with deep mantle slab-driven flow contribute more than 90% of the total driving forces while the remaining driving forces, coming from the push due to thickening of oceanic plates at the mid-ocean ridges, contribute less than 10%. In contrast, lower values of about 50% to 70% as the slab pull contribution to the total force balance of global plate motions were reported in other studies (Becker & O'Connell, 2001; Conrad & Lithgow-Bertelloni, 2002). Also, these studies often ignore the influence of slab bending resistive force, which has been the focus of Wu et al. (2008), and the effect of non-convective forces due to topography in oceans and continents (Bercovici et al., 2000), both of which we take into account using our numerical method including an upper boundary free surface and the effect of self gravitation (see section 2).

Although it is generally acknowledged that subduction influences global plate velocities (Forsyth & Uyeda, 1975; Hager & O'Connell, 1981), the contribution of a subducting plate is also influenced by factors such as plate boundary friction, slab viscosity and the asthenosphere viscosity (Alisic et al., 2012; Davies, 1978; Tan et al., 2012; van Summeren et al., 2012), making a quantification of the slab pull contribution challenging. Geodynamic modeling studies of global plate motions often ignore the frictional resistance to the slab pull force at shallow depths (e.g., Conrad & Lithgow-Bertelloni, 2004; van Summeren et al., 2012) or quantify it with the aid of slab bending force (e.g., Wu et al., 2008), and only few studies have explored the importance of friction or plastic stress yielding at plate boundaries (e.g., Crameri & Tackley, 2015; Stadler et al., 2010). In this study, we explore the combined influence of plate boundary friction (plastic yielding) and asthenosphere viscosity on plate motion. The stress distribution along subducting plates due to slab pull and/or deep slab suction is influenced by the frictional force at shallow depths (Davies, 1978). The frictional resistance between subducting and overriding plates is of the order of tens of MPa (Lamb & Davis, 2003; Sobolev & Babeyko, 2005), giving rise to crustal and/or lithospheric deformation such as observed in the Andes, Himalayas and San Andreas faults. Sobolev and Babeyko (2005) explored the effect of frictional strength of the subduction interface on surface topography at active margins. They concluded that forming such tectonic features as observed in nature requires low friction, with a coefficient of static friction (μ) within the range of 0.01 to 0.1 (friction angles 1° to 15°) compared to a much higher value of $\mu \sim 0.6$ according to Byerlee's Law (Byerlee, 1978) for dry rocks and also values in the plate interior (Zhong & Watts, 2013). Similarly, low values of friction coefficient have been suggested for the San Andreas Fault systems and the Andean subduction zone (Bird & Kong, 1994; Carena & Moder, 2009; Humphreys & Coblentz, 2007; Iaffaldano et al., 2006; Mount & Suppe, 1987; Townend & Zoback, 2004; Zoback et al., 1987). Previous numerical models (Crameri & Tackley, 2015; Moresi & Solomatov, 1998; Richards et al., 2001; Tackley, 2000a) have shown as well that the use of smaller coefficients of friction $\mu < 0.1$ (yield stress 100 MPa) would lead to plate tectonics in models of mantle convection.

Furthermore, numerical modeling of subduction (Becker & Faccenna, 2009; Gurnis et al., 2004; Hall et al., 2003; Hassani et al., 1997; Kaus et al., 2008; Sobolev & Babeyko, 2005; Sobolev et al., 2006) has demonstrated that low coefficients of friction at the subduction interface are required to sustain subduction ($\mu < 0.1$). At shallow depths ($\sim$60 km), where brittle deformation occurs (Oleskevich et al., 1999; Schwartz & Rokosky, 2007), friction plays an important role at subducting margins. At greater depths with high temperatures, viscosity becomes an important parameter controlling plate motions (Bercovici & Richards, 2000). Using a 2D self-consistent dynamic model, the study of Crameri and Tackley (2015) has shown that treating plate boundaries with visco-elasto-plastic rheology enables subduction initiation. We treat our plate boundaries in a similar fashion to explore the influence of the friction coefficient on global plate motions. Such combined frictional and viscous treatment of plate boundaries is more realistic compared to previously suggested approaches using low-viscosity/weak zones (e.g., Becker, 2006; Gérault et al., 2012; Zhong et al., 2000) at plate boundaries.

Below the brittle layer, we have implemented a complex upper mantle rheology due to temperature increase with depth and the presence of cold slabs and cratons. To date, many numerical modeling studies have employed an over-simplified treatment of the complex upper mantle rheology and its effects on the magnitudes and directions of plate velocities using either a simplified (i.e. layered/radial) viscosity structure

of the upper mantle or a parameterization of the other rheological/force contributions to match the surface observables such as plate motion (e.g., Becker & O'Connell, 2001; Conrad & Lithgow-Bertelloni, 2002; Lithgow-Bertelloni & Silver, 1998; Steinberger et al., 2001). In contrast, the nonlinear viscosity of the upper mantle arising from cold dense subducting plates (Burov, 2011; Faccenna et al., 2007), deeply penetrating cratonic roots of continents (Karato, 2010), and a wide range of temperature regimes has been the focus of other more advanced modeling studies of global mantle convection in relation to plate motions (Alisic et al., 2012; Becker, 2006; Ghosh & Holt, 2012; Stadler et al., 2010; van Summeren et al., 2012; Zhong & Gurnis, 1996; Zhong et al., 2000). For example, Stadler et al. (2010) and Alisic et al. (2012) have found that the slab pull force in the upper mantle is better transmitted to the subducting oceanic plate, if non-linear rheology of slabs is considered. Although these numerical studies have analyzed the rheological implications of each driving or resisting force on the overall plate motions, they often simplified or even neglected some critical aspects of the upper or lower mantle dynamics. To fully account for all the plate motion driving forces, a modeling approach must include visco-elasto-plastic rheology of the upper mantle.

The total balance of plate motion forces arising from subducting slabs, continental keels, viscous shearing of the asthenosphere, plate boundary yielding and/or strain-weakening may also cause the development of net rotation (NR) of the lithospheric plates with respect to the deep mantle (Becker & Faccenna, 2009; O'Connell et al., 1991; Ricard et al., 1991; Zhong, 2001). The NR of the lithospheric plates originates from toroidal flow due to pertaining lateral viscosity variations (LVVs) in the mantle (Bercovici & Richards, 2000; O'Connell et al., 1991; Ricard et al., 1991). Previous numerical studies that used NR to constrain mantle rheology (Becker, 2006; Zhong, 2001) have shown that the largest contribution to lithospheric NR comes from the uppermost $\sim$400 km of the mantle. For example, Zhong (2001) has shown that NR is mainly influenced by the continental keels ($\sim$80 %), the deepest of which are placed by modern seismic imaging techniques and xenolith studies in the depth range of 200–300 km (Artemieva & Mooney, 2002; Carlson et al., 2005; Griffin et al., 2004; Gung et al., 2003; Yuan & Romanowicz, 2010). A similar conclusion was obtained by Becker (2006) who explored relative contributions of different mantle rheologies at different depths to lithosphere NR in global 3-D mantle flow models with both free-slip and prescribed dynamic upper mantle conditions. We explore the influence of LVVs within the top 300 km of the upper mantle on the NR of the lithospheric plates with a free surface at the top boundary in our numerical model.

The decoupled motion of the rigid lithospheric plates over the weak asthenosphere is also believed to be a consequence of the presence of water (Hirth & Kohlstedt, 2004; Karato & Wu, 1993) giving rise to a weakening of the asthenosphere by more than 2 orders of magnitude compared to dry mantle materials. Presence of water in the asthenosphere has been documented by experimental studies using magma samples from mid-ocean ridges. They have shown that at spreading plate boundaries magma contains about 0.1 - 0.3 wt % of water (Danyushevsky et al., 2000; Michael, 1995; Sobolev & Chaussidon, 1996) that corresponds to water content in the mantle of 0.01–0.03 wt %. At convergent boundaries the water content in the mantle is higher, exceeding 0.1 wt % (Sobolev & Chaussidon, 1996). Here we explore the effect of asthenospheric creep viscosity on plate motions, using wet and dry olivine parameters inferred from laboratory experiments and our setup for a 3-D thermal structure of the upper mantle (see section 2.2). We do this using a global Earth model, where deformation in the upper 300 km is computed with the 3-D finite-element numerical technique SLIM3D (Popov & Sobolev, 2008) with visco-elasto-plastic rheology, coupled to a spectral mantle flow code (Hager & O'Connell, 1981) at 300 km depth. We show that matching the observed plate motion requires the use of much lower friction coefficients at plate boundaries than suggested in the majority of mantle convection modeling studies, namely $\mu < 0.1$ (Crameri & Tackley, 2015; Moresi & Solomatov, 1998; Richards et al., 2001; Tackley, 2000a). We also explore the combined influence of plate boundary friction and asthenosphere viscosity on the magnitude and location of the net rotation (NR) Euler pole of the lithospheric plates.

2. Methods

2.1. Model Description

In this section we give a brief description of our coupled numerical model of mantle flow and deformation within the crust and lithosphere. The upper component is modeled through the particle-in-cell finite element, thermo-mechanical numerical code SLIM3D (3-dimensional lithosphere-asthenosphere code) of Popov and Sobolev (2008) that solves the energy and momentum equations using an arbitrary-Lagrangian-

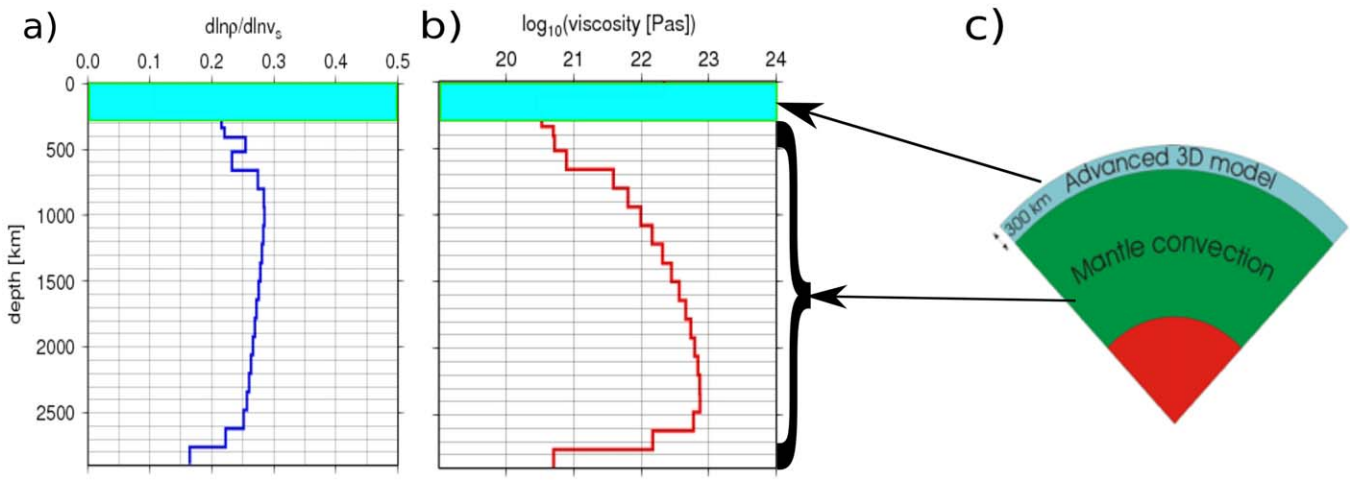

Figure 1. (a) Depth-dependent scaling profile of s-waves velocity to density; (b) radial mantle viscosity structure (Steinberger & Calderwood, 2006) and (c) a schematic diagram of the numerical method coupling the upper mantle 3-D -lithosphere-asthenosphere code SLIM3D (Popov & Sobolev, 2008) to a lower mantle spectral mantle flow code (Hager & O'Connell, 1981) at a depth of 300 km.

Eulerian grid with a Winkler boundary condition at the base and a true free surface upper boundary condition. This code has been extensively benchmarked by Popov and Sobolev (2008) with respect to various deformational processes within the crust and lithospheric mantle and also has been used in other studies focusing on lithospheric deformation processes (Brune et al., 2012, 2014, 2016; Quinteros & Sobolev, 2013). For this study we use an extention of the SLIM3D code to a global scale (Sobolev et al., 2009). In that modeling technique the SLIM3D code is coupled to the spectral code of Hager and O'Connell (1981) at some prescribed depth, typically 300–400 km (Figure 1c). The top domain (SLIM3D), has 3 different layers (phases) representing the crust, lithosphere and sub-lithospheric mantle. In our simulations we assume the thickness of the upper domain to be 300 km. In this way, the upper domain consists of the crust and mantle lithosphere including all major cratonic roots, a significant portion of the sub-lithospheric mantle and at least the upper portio of the subducting slabs. Thus, it operates within the depth range, where the consideration of nonlinear upper mantle rheology and the use of high spatial resolution are most important for resolving small scale deformation processes, which may influence global plate motions.

The coupled model does not allow for a material exchange between the two model components but requires continuity of tractions and velocities at the interface. Tractions in the lower mantle are first computed using the spectral mantle convection model component with a 3-D density structure inferred from the hybrid seismic tomography model of Becker and Boschi (2002) using a velocity-to-density conversion profile (Figure 1a) and a radial mantle viscosity profile (Figure 1b), both from Steinberger and Calderwood (2006). Tractions computed by the spectral model, both the normal τ_{rr} and the shear $\tau_{r\theta}$ and $\tau_{r\phi}$ components, are then passed to the lithosphere-asthenosphere model as a dynamic boundary condition within a Newton-Raphson iteration procedure. At each iteration step, we prescribe mantle flow-derived tractions as a lower boundary condition in SLIM3D, and compute the flow velocities in the upper (SLIM3D) domain. Computed flow velocities at the lower boundary of the upper domain are in turn passed back to the spectral model component as an upper boundary condition.

We run the coupled model forward in time for half a million years with a time step of $5 \cdot 10^4$ years. The convergence is evaluated by comparing the velocity and traction norms of two successive iterations at 300 km depth up to spherical harmonic degree 63. For every Newton-Raphson iteration step, we estimate the displacement residual ratio and compare with a tolerance value set at $5 \cdot 10^{-3}$. We consider our solution converged when the estimated ratio is less than the tolerance for a time step. Since our numerical method does not account for material exchange across the coupled interface, time evolution longer than 2 Ma creates numerical instability; for example, sinking slabs in the top 300 km cannot cross the coupled interface. Hence, we restrict our simulations to $5 \cdot 10^5$ years time-dependent evolution to predict present-day plate velocities in contrast to instantaneous calculations (e.g., Alisic et al., 2012). The iterations between both coupled components within a time step are considered converged if the

norms between successive velocities remain almost the same. At each time step we calculate the net rotation of the lithosphere and plate velocities in the no-net-rotation reference frame. This study's modeling technique is also complemented with the calculation of the lithosphere stress field and dynamic surface topography (Osei Tutu et al., 2017), which are used to evaluate the influence of the crustal and upper mantle heterogeneities on the observed lithosphere stress field and the corresponding topography beneath air.

2.2. Upper Mantle Rheology and Thermal Structure

The coupling between the lithosphere and the mantle beneath in our model allows for an implementation of realistic rheological parameters in both model domains. In SLIM3D, the stress- and temperature-dependent rheology is implemented according to an additive strain rate decomposition into the viscous, elastic and plastic components:

$$\dot{\varepsilon}_{ij}=\dot{\varepsilon}_{ij}^{vis}+\dot{\varepsilon}_{ij}^{el}+\dot{\varepsilon}_{ij}^{pl}=\frac{1}{2\eta_{eff}}\tau_{ij}+\frac{1}{2G}\hat{\tau}_{ij}+\dot{\gamma}\frac{\partial Q}{\partial\tau_{ij}} \tag{1}$$

where G denotes the elastic shear modulus, $Q=\tau_{II}$ is the plastic potential function, $\hat{\tau}_{ij}$ is the objective stress rate, $\dot{\gamma}$ denotes the plastic multiplier, $\tau_{ij}=\sigma_{ij}+P\delta_{ij}$ is the Cauchy stress deviator, $P=-\sigma_{ii}/3$ is the pressure, $\tau_{II}=(\tau_{ij}\tau_{ij})^{1/2}$ stands for the effective deviatoric stress, and η_{eff} is the effective creep viscosity derived by combining the diffusion and dislocation creep mechanisms, as follows:

$$\eta_{eff}=\frac{1}{2}\tau_{II}(\dot{\varepsilon}_{diff}+\dot{\varepsilon}_{disl})^{-1} \tag{2}$$

The effective scalar creep strain rates are given by Kameyama et al. (1999):

$$\dot{\varepsilon}_{diff}=A_{diff}d^{-p}(C_{H_2O})^{r_{diff}}\tau_{II}\cdot\exp\left(-\frac{E_{diff}+PV_{diff}}{RT}\right) \tag{3}$$

$$\dot{\varepsilon}_{disl}=A_{disl}(C_{H_2O})^{r_{disl}}(\tau_{II})^{n}\cdot\exp\left(-\frac{E_{disl}+PV_{disl}}{RT}\right) \tag{4}$$

where the symbols A, E and V denote the experimentally prescribed pre-exponential factor, the activation energy and the activation volume, respectively, R denotes the gas constant, T is the temperature, n is the power law exponent, d is the grain size, and p is the grain size exponent. C_{H_2O} is water content in H/10^6Si, and r_{diff} and r_{disl} are the water content exponents.

Within the top 300 km (SLIM3D) of the coupled model, we self-consistently account for the plastic deformation according to a Drucker-Prager criterion, based on the full dynamic pressure as opposed to using the lithostatic pressure:

$$\tau_{yield}=c+\mu P \tag{5}$$

where c is the cohesion and μ the coefficient of friction. Along the weak plate boundaries, we evaluate the influence of plastic (brittle) deformation on global plate motions by varying μ. Following Sobolev et al. (2009) we use the reduced friction coefficient values at the predefined plate boundaries (Bird, 2003) treated as narrow vertical zones in the crustal and lithospheric layer in the depth range 0–80 km, and high friction coefficient of 0.6 in all lithospheric materials outside of the plate boundaries.

The upper mantle creep viscosity is calculated using olivine parameters from the axial compression experiments of Hirth and Kohlstedt (2004). Crustal rheology is taken from Wilks and Carter (1990). All rheological parameters used in this study, except for the water content which is varied in section 3 (also see supporting information for the varying water content), are summarized in Table 1. For more details regarding the formulation of the physical model and numerical implementation the reader is referred to Popov and Sobolev (2008).

In oceans, the 3-D thermal structure for the upper 300 km is inferred from sea floor age (Müller et al., 2008). We have implemented a half-space cooling model to determine temperature T_{ocean} as a function of age and depth according to

Table 1
Parameters for the Thermo-Mechanical Modeling of the Upper Mantle Modified After Hirth and Kohlstedt *(2004)*

Parameter	Unit	Crust	Lithosphere (strong mantle)	Asthenosphere (weak mantle)
Bulk modulus , K	GPa	6.3	12.2	12.2
Shear modulus , G	GPa	4.0	7.40	7.40
Density , ρ_{ref}	gcm^{-3}	2.85	3.27	3.30
Cohesion, c	MPa	5.0	5.0	5.0
Friction coefficient, μ	-	0.6*	0.6*	0.6*
Diffusion creep parameters (p =3, d=10 mm, r = 1)				
A_{diff}	$Pa^{-1}s^{-1}$	-	$10^{-8.15}$	$10^{-8.82}$
Activation energy, E_{diff}	KJ/mol	-	375	335
Activation volume, V_{diff}	cm^{-3}/mol	-	6.0	4.0
Dislocation creep parameters Dislocation (p = 0, r = 1.2)				
A_{disl}	$Pa^{-n}s^{-1}$	$10^{-21.05}$	$10^{-13.88}$	$10^{-13.52}$
Activation energy, E_{disl}	KJ/mol	445	530	480
Activation volume , V_{disl}	cm^{-3}/mol	10.0	17.0	14.0
Power law exponent, n	-	4.2	3.0	3.0

Note. Olivine water content used for our viscosity profiles 100, 200, 500, 800, 1000 H/10^6Si in the weak mantle (asthenosphere), which is included in the pre-exponential factor for olivine, with dry lithospheric parameters. The creep parameters for the crust are given by *Wilks* (1990]. (*Away from plate boundaries).

$$T_{ocean}(z,\tau)=T_s+(T_m-T_s)\,\mathrm{erf}\left(\frac{z}{2\sqrt{k\tau}}\right) \tag{6}$$

where $k=8\cdot10^{-7}$ m^2s^{-1} is thermal diffusivity, τ is the age of the oceanic lithosphere, T_s is the reference surface temperature, T_m is the reference mantle temperature and z is depth below the surface. It is combined with the TC1 model (Artemieva, 2006) in continents, which is based on a compilation of heat flow data. We account for slabs in the upper mantle (300 km), using slab locations and depths from Steinberger (2000) and the slab age with equation (6) to infer a corresponding temperature field. In Figure 2, slices of the inferred thermal structure for the upper mantle at depths of 50, 100, 150 and 250 km show cratons and slabs as the coldest structures and ridges with the highest temperatures. For our modeling setup, we used reference crustal, lithospheric and asthenosphere densities (Table 1) and accounted for lateral density variations from our 3-D thermal structure (Figure 2) using the relation:

$$\rho(\Delta T)=\rho_{ref}\left[1-\alpha\Delta T+\frac{P}{K}\right] \tag{7}$$

where α is the thermal expansivity coefficient, chosen to be $3\cdot10^{-5}$ K^{-1} within the lithospheric and asthenospheric mantle, K (Table 1) is the bulk modulus and ρ_{ref} the reference density at reference temperature (20°C) and zero pressure. In the crustal layer, we use $\alpha=2.7\cdot10^{-5}$ K^{-1} with a thermal conductivity of 2.5 W/m/K and a heat production rate of 0.5 nW/kg. In both the crust and lithospheric mantle, we use the value of 1.2 kJ/kg/K for the specific heat capacity and neglect the heat production in the lithospheric mantle for our short simulation time (0.5 Ma).

2.3. Validation of the Modeling Technique

We test our modeling technique by comparing our modeling results with the results of well-established modeling techniques. First we consider models of mantle convection with radial viscosity distribution in the entire mantle, 3-D density distribution from scaling of the SMEAN tomographic model (Becker & Boschi, 2002) and free slip boundary condition at the surface and core-mantle boundary. We compute velocities using the spectral code based on Hager and O'Connell (1981) for two different viscosities in the upper 100 km and the same viscosity structure in the rest of the mantle. The resulting velocities at the surface and at depth 300 km are shown in supporting information Figures S1b and S1c (left column) and corresponding vertical cross sections of viscosity and velocities are shown in supporting information Figures S2 and S3 (left column). We then compute velocities for the same viscosity and density distributions in the mantle and the same boundary conditions but with our modeling technique that combines the SLIM3D finite element code in the upper 300 km and the spectral code deeper than 300 km (supporting information Figures S1b, S1c, S2, and S3, right column). In this case we use a

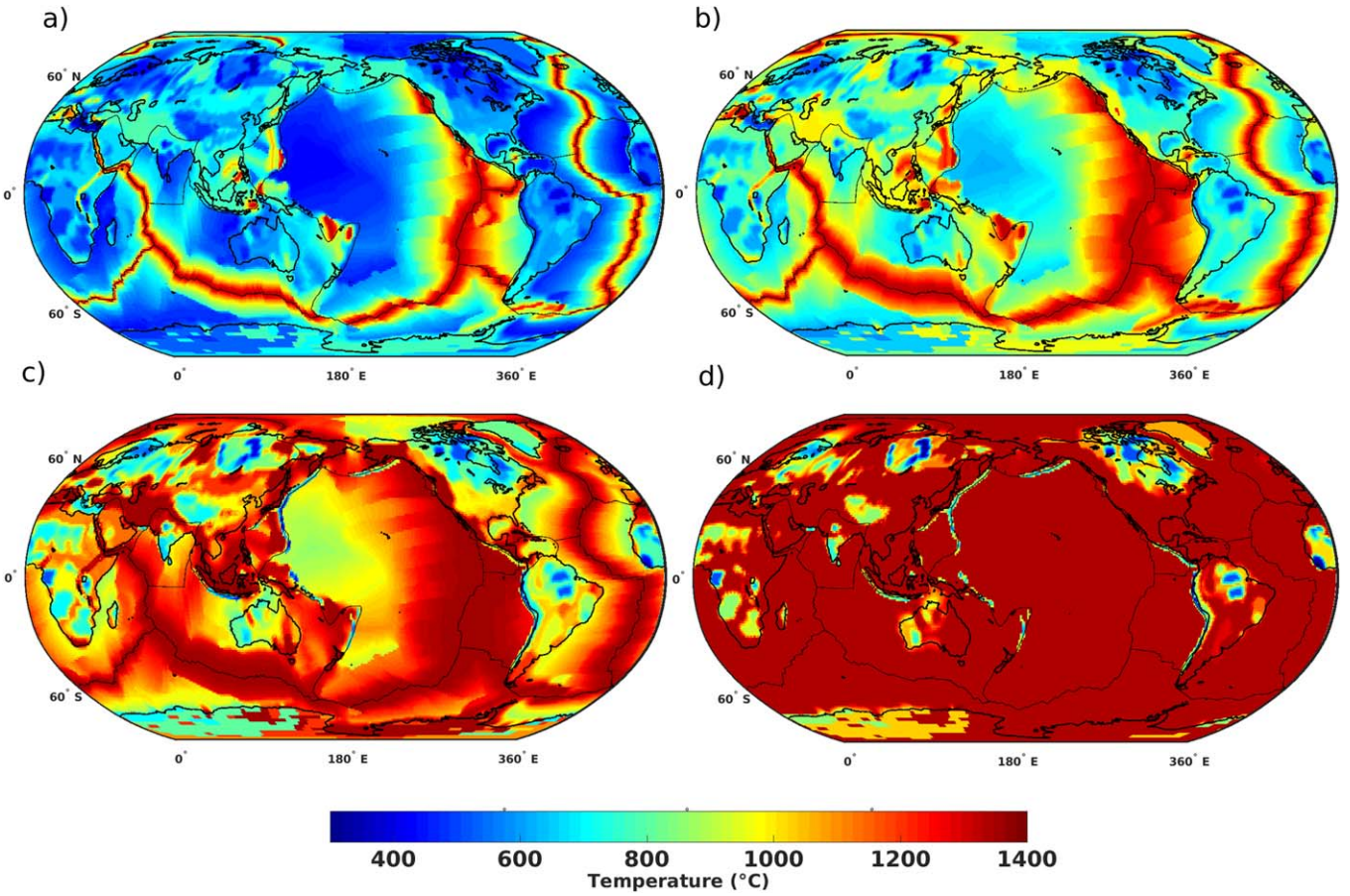

Figure 2. 3-D thermal structure at depths of (a) 50 km, (b) 100 km, (c) 150 km, and (d) 280 km, showing (a) high temperature due to mid-ocean-ridges, (b and c) cold cratonic roots in continents and d) cold subducting slabs along most convergent plate boundaries.

finite element size of 2 angular degrees obtaining the lowest RMS misfit 2% for surface velocities with lithosphere viscosity 10^{23} Pa s and the largest misfit of 8% for velocities at 300 km depth (supporting information Figure S1c). The difference between velocities computed using combined and single conventional modeling techniques is small for both viscosity structures. The vertical profiles over the Nazca and Sumatra subduction zones for both numerical techniques are very similar (supporting information Figures S2–S3).

To further test our numerical model with a 3-D viscosity structure in the upper mantle, we attempted to reproduce the model by Becker (2006) with temperature and strain-rate dependent viscosity, computed with the CitcomS code (Zhong et al., 2000). We used the same 3-D density distribution in the mantle and 3-D temperature and viscosity structure in the upper 300 km as Becker (2006) including the same low viscosity at plate boundaries. In the mantle deeper than 300 km we used a radial viscosity distribution calculated by laterally averaging the 3-D viscosity distribution of Becker (2006). Supporting information Figure S4 shows a comparison of surface velocities in the NNR reference frame of the model by Becker (2006) (red arrows) and our combined-technique model (blue color). Our model was calculated with finite element size of 1 angular degree and we ran the model for a model time of 250 thousand years. Supporting information Figure S4 shows that the surface velocities computed with two different modeling techniques are very similar. This is also true for the location of the pole of net rotation and the angular velocity of net rotation of the lithosphere (red and blue symbols and numbers in supporting information Figure S4). Interestingly, surface velocities and net rotation are almost the same in both models, although Becker (2006) has a 3-D viscosity distribution in the mantle below 300 km, while our model has only radially dependent viscosity below 300 km. From that we infer that relatively smooth lateral variations of viscosity deeper than 300 km, as in Becker (2006), affect neither the integrated tractions at the base of large lithospheric plates nor net rotation much. This justifies the assumption of radial-only dependence of viscosity in our model below 300 km depth. Another conclusion is that our combined modeling technique produces very similar results as the CitcomS code.

Finally, we test our numerical method by considering the modeling parameters from Alisic et al. (2012), with their yield stresses 100 MPa and 800 MPa and stress exponents n = 3.0, 3.5 and 3.75. The most significant observation is that as we increase the stress exponent from n = 3.0 to n = 3.5, the plates move faster, more than three fold, giving RMS velocities of 2.79 cm/yr (supporting information Figure S5, left column) and 9.57 cm/yr (supporting information Figure S6, left column) respectively, due to large strain rate weakening (Alisic et al., 2012). Resulting vertical cross sections show regions of continental keels (supporting information Figures S5 and S6, right column). However, when we increase the yield stress from 100 MPa to 800 MPa only for plate interiors without influencing plate boundaries, we observe almost no change in either magnitudes or directions of the lithospheric plate motions with RMS 2.79 cm/yr (n = 3.0, τ_{yield} = 100 MPa) and 2.78 cm/yr (n = 3.0, τ_{yield} = 800 MPa). These results suggest that plate velocities are less dependent on the strength of the plate interior, but largely on how easily the boundaries can deform, as they move relative to each other. We believe that the tests described above demonstrate that our combined modeling technique is robust and is able to reproduce modeling results of well-established modeling techniques.

3. Results and Discussion

3.1. Average Creep Viscosities and Corresponding Basal Tractions

First we compute a global dynamic geoid model and basal shear tractions at 300 km (Figures 3b and 3d) to ascertain that our upper mantle lateral viscosity variations yield realistic results. Then we compare the predicted geoid to an estimate from the layered/radial viscosity (η_r) model of Steinberger and Calderwood (2006) and the observed GRACE geoid model (supporting information Figures S7a–S7c). In Figure 4b, we

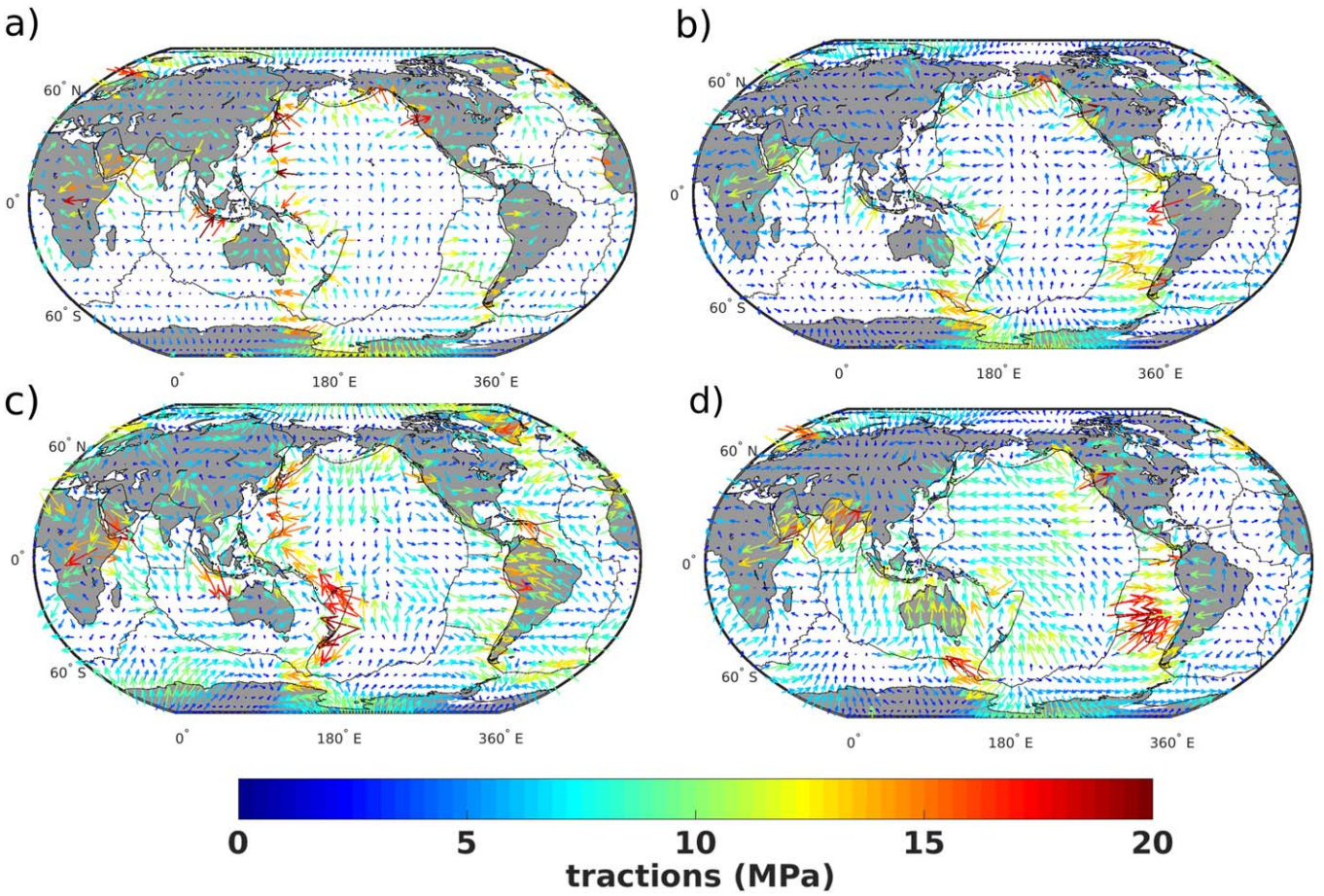

Figure 3. (a) Predicted basal tractions at 300 km with a layered viscosity structure (Steinberger & Calderwood, 2006) and (b) lateral viscosity variations from olivine parameters consistent with the depth averaged creep viscosity profile in Figure 4 (the pink line 500 H/10^6Si) with μ=0.03 along plate boundaries. (c and d) The same with one order of magnitude lower viscosity in the asthenosphere, with μ=0.03 at ocean-continent subducting regions and μ=0.01 at the remaining plate boundaries. The predicted geoid models corresponding to a) and b) are shown in supporting information Figure S7.

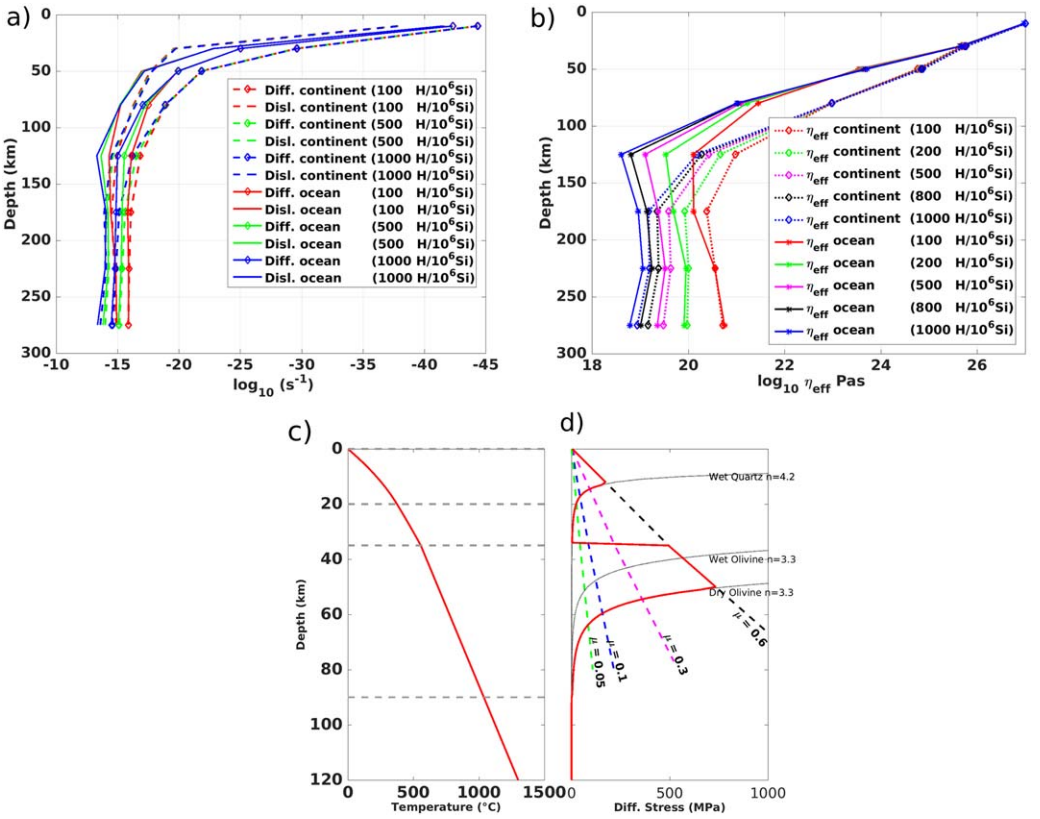

Figure 4. (a) Calculated average strain rate versus depth for diffusion and dislocation creep across continents and oceans. (b) The corresponding average creep viscosity versus depth in the upper mantle with olivine parameters. (c) Reference temperature profile within the crust and lithospheric layers and (d) Yield strength profile using frictional coefficient $\mu \sim 0.6$ as inferred for dry rocks from laboratory experiments (Byerlee, 1978) and smaller frictional coefficients with $\mu \sim 0.1$ as suggested by numerical simulations (Moresi & Solomatov, 1998) used as an upper limit for the plate boundaries.

show profiles of the resulting creep effective viscosity for continents and oceans within the top 300 km using the creep parameters given in Table 1 (see supporting information Table S1–S5) and our 3-D upper mantle thermal structure (Figure 2). The corresponding diffusion and dislocation creep estimates are shown in Figure 4a. We have conducted a series of experiments by varying the water content in the asthenosphere (C_{H_2O}) within the following set: 100, 200, 500, 800, 1,000 ppm H/10^6Si. Figure 4b, shows how the average asthenospheric viscosity decreases with water content (Green et al., 2010; Karato, 2010).

In general, all oceanic average viscosity profiles lie below their respective continental average effective viscosity (η_{eff}), within the 100±60 km depth range, which is broadly consistent with the mean depth of the oceanic asthenosphere. This depth range of low oceanic viscosity (Figure 4b) corresponds to a seismic wave velocity drop ($\sim$ 5–10%) in most recent seismological studies showing the transition between lithosphere and asthenosphere (e.g., Fischer et al., 2010; Kawakatsu et al., 2009; Rychert et al., 2005; Schaeffer & Lebedev, 2013). The difference between the averaged ocean and continent viscosity profiles in the depth range of 100±60 km is $\sim$1 order of magnitude. We obtain the lowest average viscosity of $\sim 5 \cdot 10^{18}$ Pas for 1000 ppm H/10^6Si olivine beneath oceans. Figure 3 shows basal tractions causing plate motions and stresses in the lithosphere for some representative cases; the resulting geoid with prescribed rheology is shown in supporting information Figure S7b. In Figures 3a and 3c only radial viscosity variation (Steinberger & Calderwood, 2006) is considered, whereas in Figures 3b and 3d the creep parameters corresponding to the effective viscosity profile in Figure 4b (blue profile) are used, with yield stress adjusted with the coefficient of friction μ=0.03 (Figure 4d) within the crust and lithospheric layer above depth 80 km for all plate boundaries. The influence of the frictional parameter at plate boundaries will be discussed in the following sections with regards to global plate motions. The predicted geoid with LVVs (supporting information Figure S7b) when compared with the observed geoid (Reigber et al., 2005; supporting information Figure S7a)

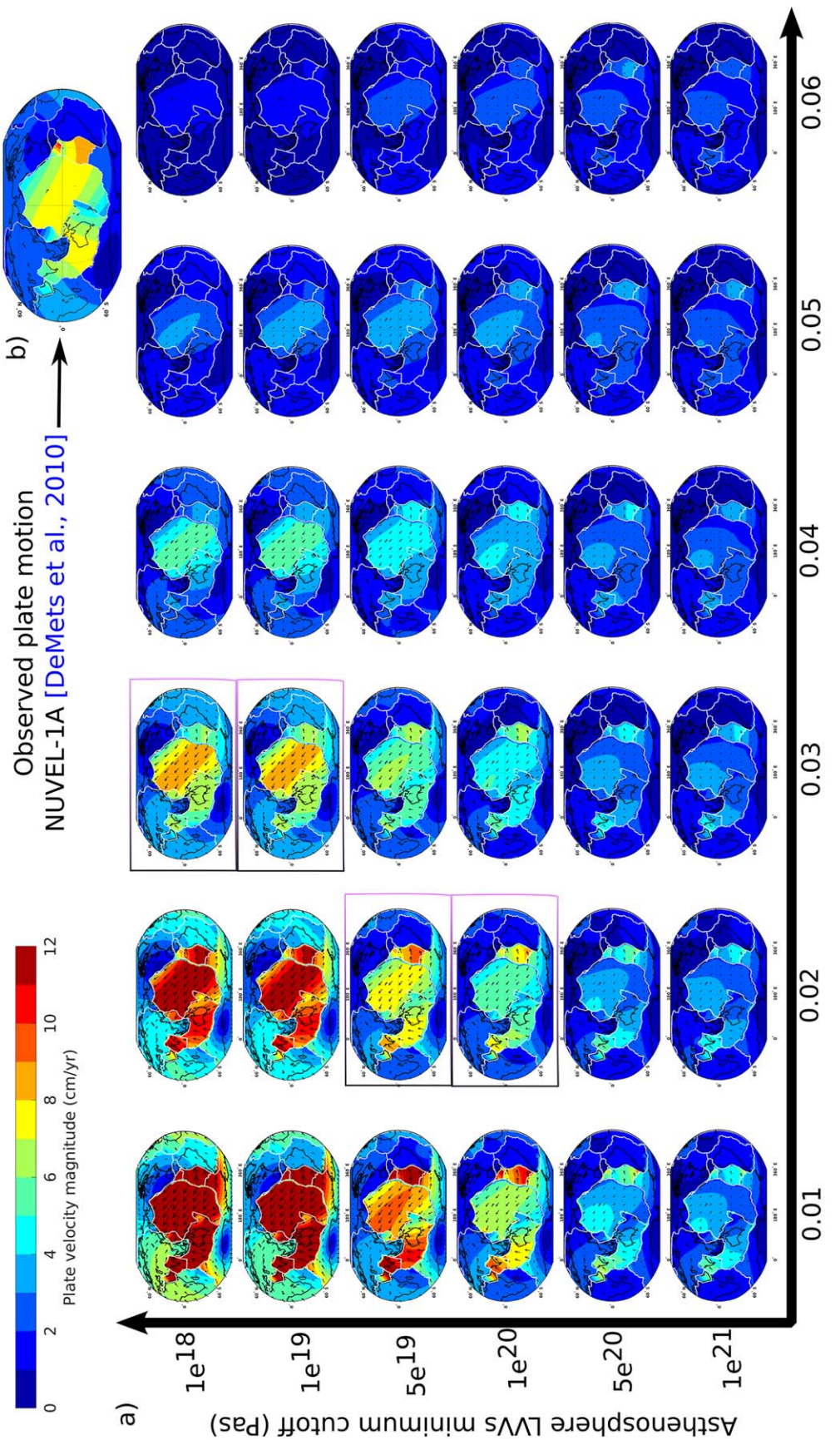

Figure 5. (a) Set of predicted plate motions with an increasing friction coefficient (plastic yielding) at plate boundaries for different minimum viscosity cutoffs of the asthenospheric LVVs with olivine parameters corresponding to the blue profile in Figure 4. We show here plate motions with coefficient of friction up to 0.06. The rectangular boxes in Figure 5a show the best fit to the observed plate motion data shown in (b) (DeMets et al., 2010).

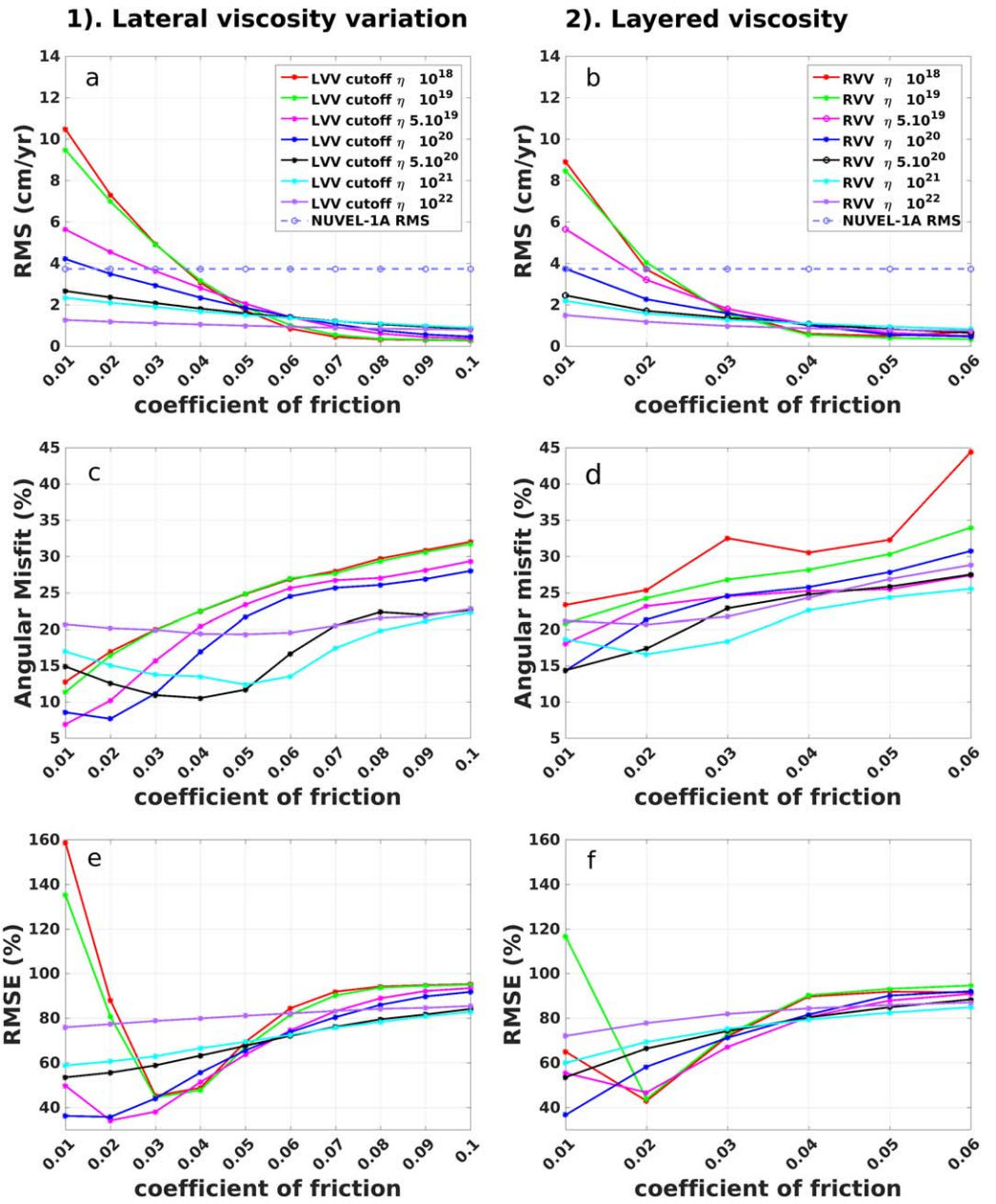

Figure 6. Estimates of global root mean square (RMS) of predicted plate motions with (a) LVVs and (b) layered viscosity in the top 300 km for different coefficients of friction compared to the observed rms velocity of NNR-NUVEL-1A (DeMets et al., 2010), (c and d) their respective global angular misfits. e and f) The root mean square error (RMSE) for the velocity in percent. Viscosity cutoff η in Pa s.

Table 2
Summary of the Upper Mantle Viscosity for Different Simulations

Upper mantle	Lateral viscosity variation (Pas)	Layered viscosity variation (Pas)
1. Lithosphere layer		
a. *variable thickness*	η_{eff} max cutoff = 10^{24}	10^{24}
b. *uniform thickness* (60, 80, 100 *and* 150 km)	η_{eff} max cutoff = 10^{24}	
2. Asthenospheric layer	η_{eff} min cutoffs = 10^{18} – 10^{21}	$\eta(z) = 10^{18}$ – 10^{21}

yields a correlation of 0.85, which is higher than the correlation of 0.82 obtained with the radial viscosity profile (Figure 1b). High geoid signal above the Andes and low signal in continental Europe and North America were reproduced quite well with the LVVs model.

3.2. Plate Motions

We use our coupled model to predict global plate motions (Figure 5), following the upper mantle creep parameters derived with lithospheric basal tractions (examples are shown in Figure 3) and a free surface as the top boundary condition. We seek to understand how

plate boundary frictional deformation and asthenosphere viscosity influence global plate velocities. To compute global plate motions in a NNR reference frame, we explore both a layered/radial viscosity structure and LVVs for the upper mantle. For LVVs we first test olivine parameters (Table 1) corresponding to the blue average creep viscosity profile (Figure 4b). We use a fixed maximum and variable minimum viscosity cutoff in the top 300 km (see section 3.4) and a prescribed yield stress (coefficient of friction) (Figure 4d) at plate boundaries. The predicted global plate motions (Figure 5) are compared with the observed plate motion model NUVEL-1A (DeMets et al., 2010) in a NNR reference frame. We compare the global root mean square (rms) velocity (Figures 6a and 6b) and the angular misfits (Figures 6c and 6d) between the modeled and observed plate motions for different values of the plate boundary friction coefficient due to plastic yielding and asthenospheric cutoff viscosity. Here we used a variable lithosphere thickness (Table 2) with our stress and strain-rate dependent viscosity and a 3-D temperature structure for the upper mantle (discussed above in section 2.2) to predict our first set of plate velocities. Our second set of predicted plate motions is based on a Newtonian/layered viscosity structure (Steinberger & Calderwood, 2006) at all depths. Our calculation with layered/radial viscosity for the upper mantle is similar to previous geodynamic modeling studies of plate motions (Becker & O'Connell, 2001; Lithgow-Bertelloni and Richards, 1998), but in contrast to either imposing surface plate velocity (Becker, 2006; Becker & O'Connell, 2001) or using weak zones with a viscosity drop (Becker, 2006; Conrad & Lithgow-Bertelloni, 2006) we have imposed plastic yielding at the plate boundaries for a dynamically self-consistent generation of plate-like surface motion.

3.3. Influence of Plate Boundary Friction on Plate Velocities

The lithospheric plate driving force coming from slab pull within the upper mantle (Conrad & Lithgow-Bertelloni, 2002, 2004; Forsyth & Uyeda, 1975; Harper, 1975; van Summeren et al., 2012) and deep mantle slab suction are broadly evident in all subducting surface plates, when we use a very low plate boundary friction $\mu < 0.04$ (Figure 5) and a relatively low asthenosphere viscosity. The Pacific plate, Nazca plate, Indo-Australian plate and Cocos plate are all moving with a maximum speed up to $\sim$ 20 cm/yr. On the other hand, non-subducting oceanic plates are moving with a relatively low velocity $\sim$5 cm/yr, and are mainly driven by either ridge push or gravitational sliding of the oceanic plate (Artyushkov, 1973; Conrad & Lithgow-Bertelloni, 2002; Harper, 1975; McKenzie, 1972) or slab suction from below 300 km, with the same low coefficient of friction $\mu < 0.04$ at plate boundaries and low asthenospheric viscosity. When we increase the resistive force due to friction by increasing the coefficient of friction at plate boundaries while keeping the same asthenospheric viscosity, we observe a corresponding decrease in lithospheric plate speed for all plates, which is more pronounced in subducting plates. For example, with a minimum asthenosphere viscosity cutoff 10^{18} Pas rms plate motion speed decreases by about 2 cm/yr for an increase of the coefficient of friction by 0.01 leading to an increase in yield stress (Figures 5 and 6a). This brings lithospheric plates to an almost stagnant lid regime as we move toward higher coefficients of friction $\sim$0.1 (Crameri & Tackley, 20152014, 2015), thereby resisting almost all of the total driving force due to slabs and basal traction. With higher coefficient of friction $\sim$0.1 the yield stress at plate boundaries is mostly not reached, even with the lowest asthenospheric viscosity 10^{18} Pas. This corresponds to a general decrease in the predicted rms global plate velocities (Figure 6a) as we increase the coefficient of friction from 0.01 (friction angle $\sim 1^{\circ}$) to 0.1 (friction angle $\sim 15^{\circ}$) for all minimum viscosity cutoffs. A similar gradual decrease in global rms velocities is obtained with layered viscosity models (Figure 6b).

Previous studies (e.g., Wu et al., 2008) have considered the slab bending force at subduction zones, and have arrived at similar conclusions on the effect of the resistive forces between subducting and overriding plates. The older is the subducting plate, the thicker it is and the stronger is the slab pull force. Hence, at intermediate coefficients of friction (e.g., 0.02, 0.03, and 0.04 for cutoff viscosity of 10^{18} Pas, Figure 5) young, thin subducting plates (e.g., Nazca and Cocos) move much slower, since the smaller slab pull does not tend to cause plastic yield. In contrast, it is easier for older, thicker plates (such as the Pacific) to achieve yielding and thus to move relatively fast. On the other hand, older plates become comparatively slower as we increase the asthenospheric viscosity while keeping the same coefficient of friction (see section 3.4).

Our findings that low friction coefficient $\mu < 0.05$ (low friction angle $<8^{\circ}$) is required at plate boundaries to generate global plate motions in a realistic fashion is consistent with previous studies (Crameri & Tackley, 2015; Faccenda et al., 2009; Hall et al., 2003; Hassani et al., 1997; Sobolev & Babeyko, 2005; Tan et al., 2012) that have considered the influence of frictional parameters on the subduction interface and numerical studies of global plate motions with plastic yielding at plate boundaries (Crameri & Tackley, 2014; Stadler et al.,

2010). In contrast, the coefficient of friction $\mu \sim 0.02$ at plate boundaries from our preferred model is much lower than the value of ~ 0.1 suggested by previous numerical studies of mantle convection (Moresi & Solomatov, 1998; Richards et al., 2001; Tackley, 2000a). The weak nature of plate boundaries that is required for plate motions (Iaffaldano et al., 2006), as well as subduction and fault systems (Bird & Kong, 1994; Carena & Moder, 2009; Humphreys & Coblentz, 2007; Mount & Suppe, 1987; Townend & Zoback, 2004; Zoback et al., 1987), compared to high values of yield stresses observed in the plate interior (Zhong & Watts, 2013), is also supported by observational constraints from heat flow data at plate boundaries (Gao & Wang, 2014) showing the different behavior of the lithospheric plates in their interior and at their boundaries. Our estimated friction coefficients are close to values (0.01 - 0.05) derived from models of subduction orogeny in the Andes (Sobolev & Babeyko, 2005).

3.4. Influence of the Asthenosphere Viscosity Structure on Plate Velocities

The second quantity that is varied in our simulations (Figure 5) is the viscosity contrast between the lithosphere and the asthenosphere, with minimum asthenosphere viscosity cutoff values for the LVVs ranging from 10^{18} Pas to a much higher value 10^{21} Pas. The distinct nature of the asthenosphere's mineral composition and thermal structure, probably due to the process of partial melting (Karato, 2012; Schmerr, 2012) and its water content (Hirth & Kohlstedt, 1996) results in a viscosity drop with respect to the overlying lithospheric plates (Dziewonski & Anderson, 1981). The high temperatures below mid-ocean-ridges and oceanic plates contribute to partial melting leading to low values in viscosity (e.g., Figure 4b, ocean profiles) compared to the cold continental cratonic regions (e.g., Figure 4b, continent profiles) resulting in high magnitudes of lateral viscosity variations (Karato, 2012). We test the plausible minimum viscosity values of the asthenosphere to study their influence on global plate motions. The use of higher cutoff values leads to a gradual decrease in the modeled plate velocities. At low cutoffs $<10^{20}$ Pas, and low plate boundary friction ($\mu < 0.04$) both subducting and non-subducting plates move with a relatively high speed, with a predicted global rms often greater than 7 cm/yr (Figure 6a), exceeding the observed rms of ~ 3.7 cm/yr for global plate motion model NNR-NUVEL-1A (DeMets et al., 2010). For the lowest viscosity cutoffs of 10^{18} Pas and 10^{19} Pas and $\mu = 0.01$, the modeled average speed is more than twice the observed speed, giving estimates of root mean square errors (RMSE) $\sim 140-160$ % (Figure 6e, red and green lines), due to the weak mechanical coupling between the lithosphere and asthenosphere (i.e. viscous drag) and between the plates. This results in a smaller drag force exerted by the mantle on plates, allowing them to move relatively faster, even in continental regions with high resistance due to keels. Note that with the weak viscous drag at the base of oceanic plates, the strong driving force due to slab pull and mantle suction (Conrad & Lithgow-Bertelloni, 2004; Forsyth & Uyeda, 1975; Harper, 1975; Stoddard & Abbott, 1996) results in a rapid motion of the Pacific, Indo-Australian, Nazca and Cocos plates with a predicted speed of more than ~ 15 cm/yr.

Nonetheless, for low asthenosphere viscosity cutoffs of $<10^{20}$ Pas and low $\mu < 0.04$, the predicted plate motion directions are rather similar to the observed plate motion directions for NNR-NUVEL-1A (DeMets

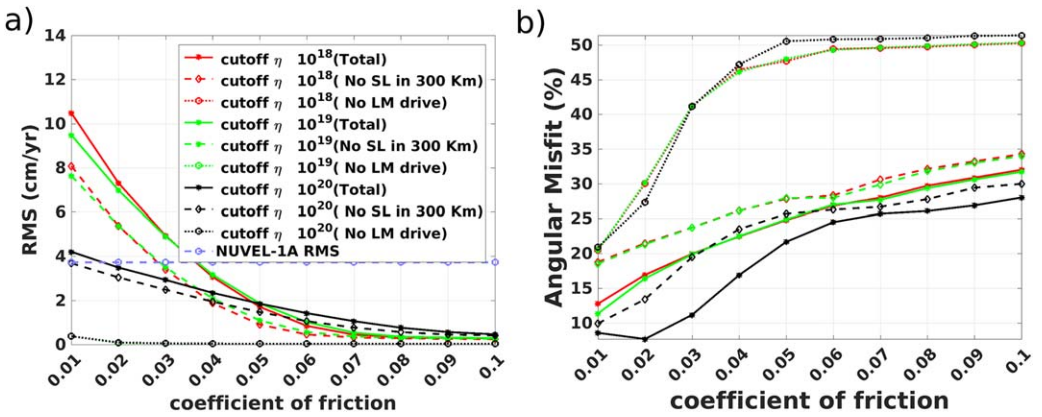

Figure 7. (a) Estimated global rms velocity and (b) angular misfit for the modeled plate motion from the simulaton including the contributions of the upper and lower mantle (Total), simulation excluding the contribution of slabs in the upper 300 km (No SL in 300 km), and those excluding the contribution of the mantle below 300 km (No LM drive). Viscosity cutoff η in Pa s.

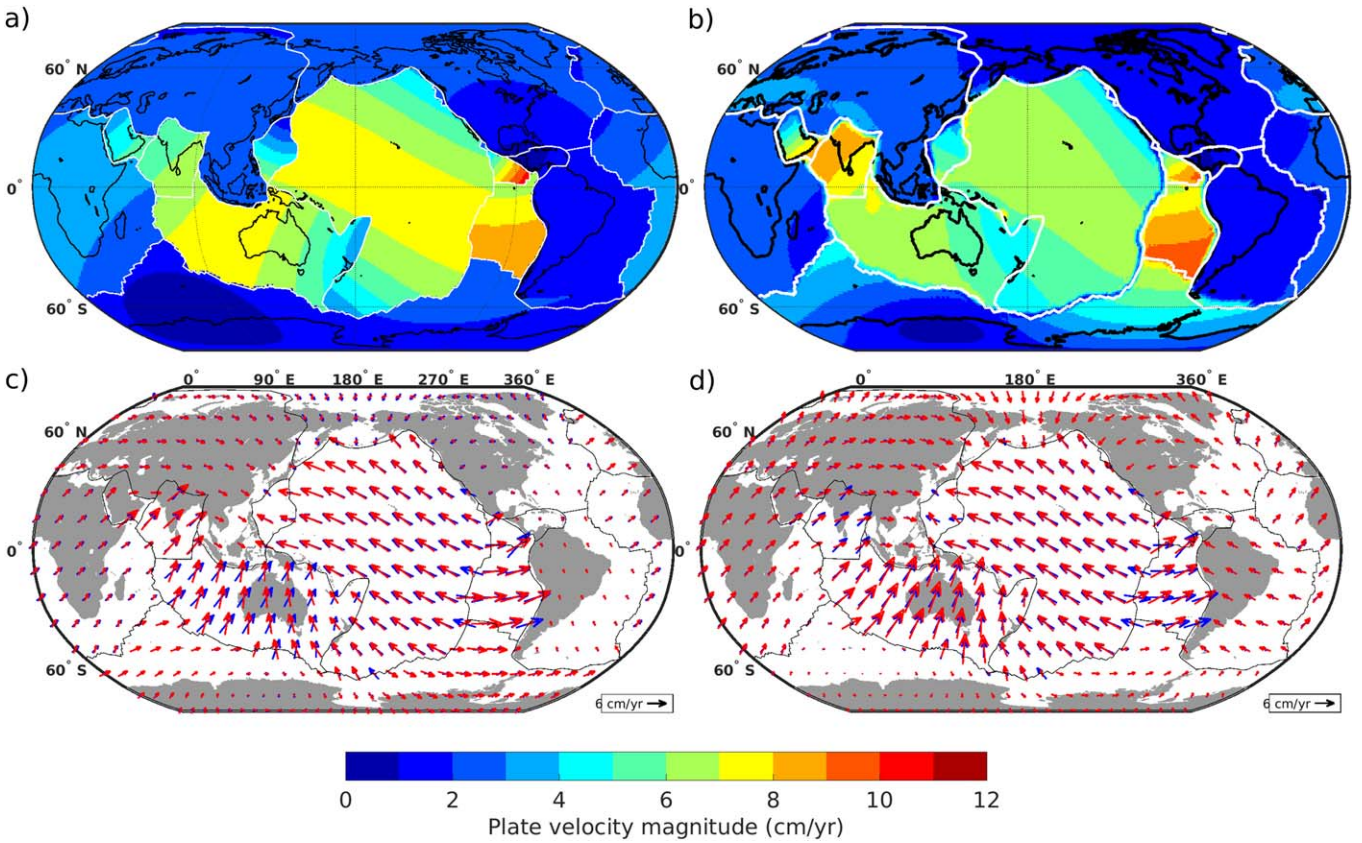

Figure 8. (a). The observed plate motion NUVEL-1A in a no-net-rotation (NNR) frame (DeMets et al., 2010). (b) Our preferred modeled plate motions (min cutoff $=10^{20}$ Pas and friction $\mu = 0.02$). (c) Direction of NUVEL-1A (blue arrows) and our preferred (red) plate motion as in (b). (d) Direction of NUVEL-1A (blue arrows) plotted on predicted (red) plate motion with min cutoff 10^{20} Pas but with $\mu = 0.0142$ (cohesion $c = 2.5$ MPa) for subducting plate boundaries and $\mu = 0.0219$ for all remaining plate boundaries.

et al., 2010) with an angular misfit $< \sim 15$ % (Figure 6e). However, as we increase the plate boundary friction coefficient to $\mu > 0.04$ while maintaining the same low asthenosphere viscosity cutoffs $<10^{20}$ Pas, the angular misfit increases and the corresponding rms velocity decreases to ~ 1 cm/yr or less, as the resistance at plate boundaries increases and plates become slower. Also, increasing the minimum asthenosphere viscosity cutoffs to $>10^{20}$ Pas deteriorates the fit for both direction (angular misfit) and magnitude (RMS) of plate motion (blue, cyan and purple profiles in Figure 6), for all coefficients of friction at plate boundaries with either LVVs or layered viscosity calculations.

We have quantified the contribution of slabs in the top 300 km of the upper mantle by removing the slabs, and obtained a decrease in the rms velocity of $\sim 20\%$ (Figure 7a) as well as an increase in the angular misfit (Figure 7b). The largest contribution comes from the mantle buoyancy below our coupling depth of 300 km providing about 70% of the driving force. The angular misfit is lowest if all contributions from the upper and lower mantle are considered (Figure 7b). In particular, angular misfit can reach 50° when we set the mantle buoyancy force to zero, thus setting all the tractions coming from the deep mantle, below our coupling interface at 300 km depth, to zero.

Our preferred model was obtained with minimum asthenosphere viscosity cutoff $=10^{20}$ Pas and $\mu = 0.02$ giving a global rms of 3.58 cm/yr and angular misfit of $\sim 8°$ (Figures 6a and 6c). In Figure 8 we have qualitatively compared this result to the NUVEL-1A plate motion model (DeMets et al., 2010) in a NNR reference frame. There is generally a good fit in terms of both magnitude and orientation, but an almost $\sim 30°$ deviation is found in Australia and more than 40° in parts of North America (Figure 8c). To achieve a better fit between the model and observations in these regions we have experimented with different coefficients of friction for subducting boundaries, transform and divergent boundaries. In Figure 8d, we have used a

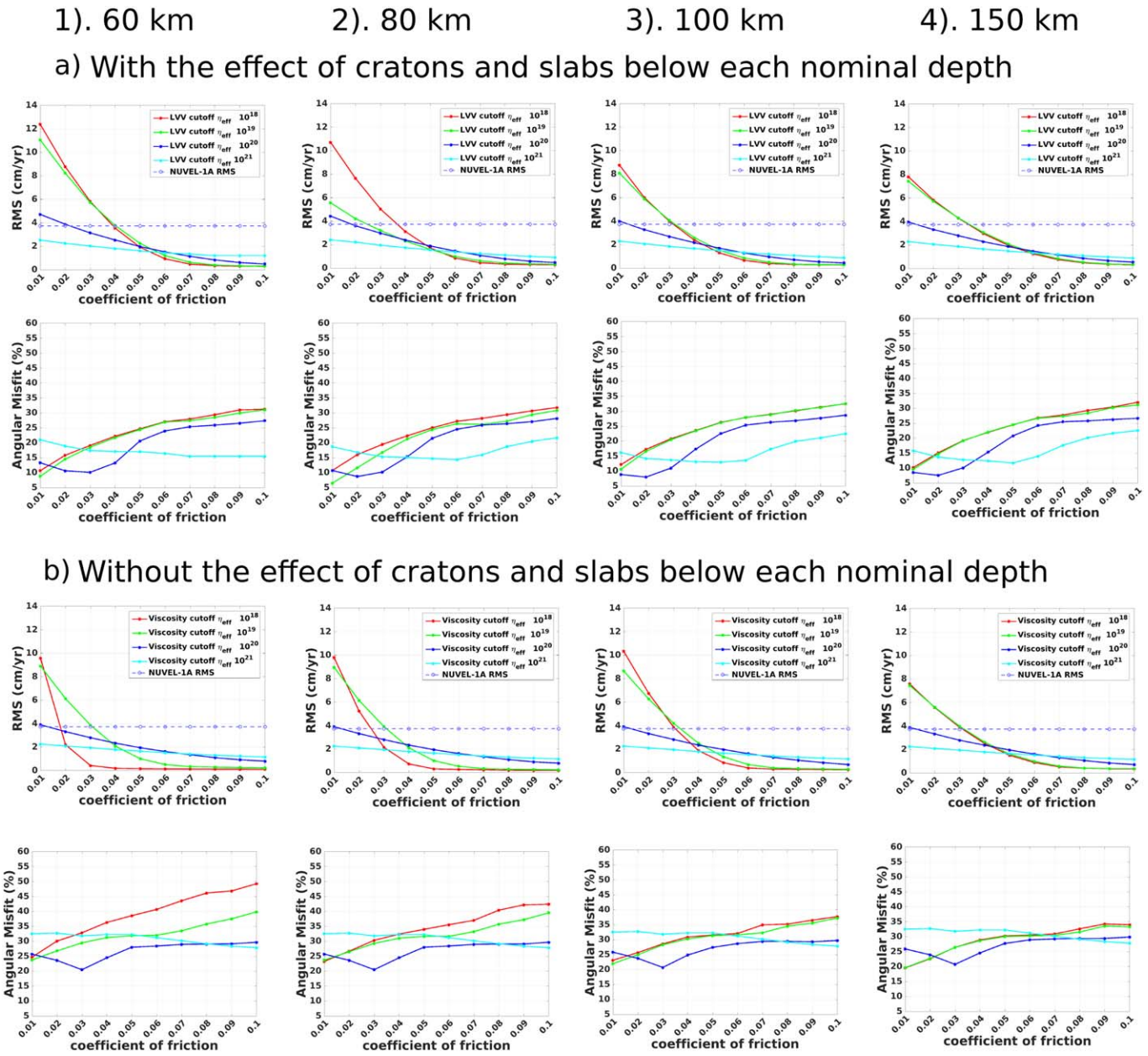

Figure 9. Modeled plate motion global rms and angular misfits for uniform lithosphere thickness of 60, 80, 100 and 150 km, (a) with and (b) without the effect of cratons and slabs below each nominal depth using plate boundary friction ranging from 0.01 to 0.1. Viscosity cutoff η_{eff} in Pa s.

minimum asthenosphere viscosity cutoff of 10^{20} Pas and $\mu = 0.0124$ for subducting plate boundaries with half the cohesion value and $\mu = 0.0219$ for all other plate boundaries. This has resulted in an improved fit to the observed plate motions in almost all regions for both magnitude and orientation. The better fit with smaller friction coefficient in subduction zones could be due to additional lubrication from sediment and water between the subducting and overriding plates as observed in nature (Lamb & Davis, 2003; Schlaphorst et al., 2016; von Huene & Ranero, 2003). However, using different friction coefficients for subducting plate boundaries and other plate boundaries has resulted in a westward motion of North and South America at a higher speed of $\sim$ 5 cm/yr and also a fit degradation for the Nazca plate.

On average, the predicted plate motions are faster (Figure 6a) with LVVs and a given asthenosphere viscosity cutoff than with the layered/radial viscosity (Figure 6b). This is due to relatively faster lateral asthenospheric flow that develops under oceanic plates (Becker, 2006), resulting from the stress and strain-rate

dependent viscosity implemented together with a 3-D thermal structure of the upper mantle. The low viscosity channel at ca. 100 km depth is seen in Figure 4b and discussed in section 3.1. Plate motion predicted with either LVVs or layered viscosity fits the observed plate velocities best when the asthenosphere viscosity is within the range of $\sim 5{\cdot}10^{19}$–10^{20} Pas underlying a lithosphere of variable thickness. This viscosity range is consistent with the values estimated by post-glacial rebound and geoid studies to constrain the upper mantle viscosity structure (Mitrovica, 1996; Mitrovica & Forte, 1997). Similar values of the asthenospheric viscosity were obtained by Cerpa et al. (2014), who studied the effect of mantle viscosity on the cyclicity of Andean slab folding.

3.5. Impact of Lithospheric Thickness on Plate Velocities

We then test our modeling setup with different values of uniform lithospheric thickness characterized by the radial viscosity of 10^{24} Pas and constant density within the lithosphere (Table 2). Our approach is similar to other modeling studies predicting global plate motions (Becker & O'Connell, 2001; Conrad & Lithgow-Bertelloni, 2002; Lithgow-Bertelloni & Richards, 1995). In the asthenosphere below each nominal lithospheric depth (60, 80, 100 and 150 km), we explore two scenarios: (I) with the presence of cratonic roots

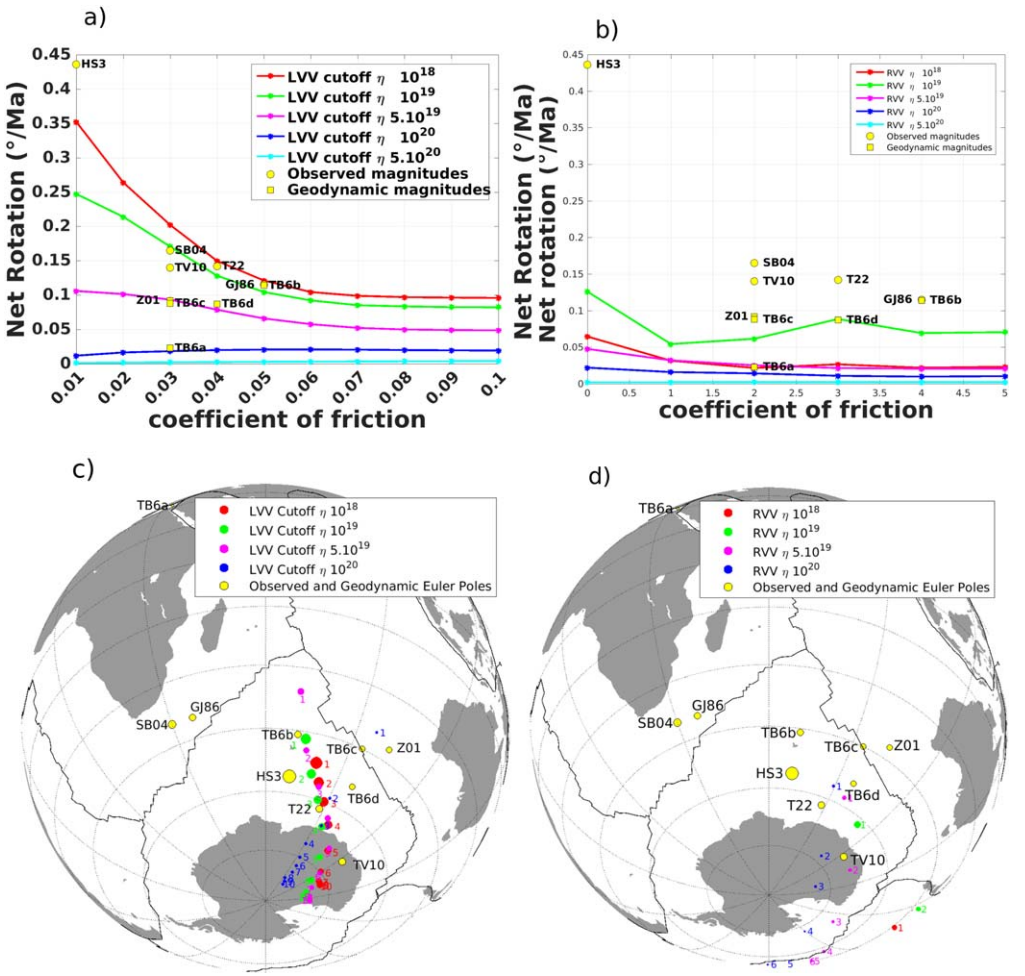

Figure 10. Net rotation amplitudes and Euler pole locations of the lithospheric plates with respect to the lower mantle for (a and c) LVVs and (b and d) layered viscosity structure. Published NR amplitudes and corresponding Euler pole locations from observation-based and previous geodynamic studies SB04 (Steinberger et al., 2004), HS3 (Gripp & Gordon, 2002), GJ86 (Gordon & Jurdy, 1986), TV10 (Torsvik et al., 2010), T22 (Wang & Wang, 2001), Z01 (Zhong, 2001) and TB6a, TB6b, TB6c and TB6 (Becker, 2006) are plotted as yellow circles and squares, respectively, with size (in Figures 10c and 10d) corresponding to amplitude. For yellow circles and squares in Figures 10a and 10b only the y-coordinate is relevant, while the x-coordinate is arbitrary. Numbers at colored circles in c and d indicate the coefficient of plate boundary friction when multiplied by 0.01. Viscosity cutoff η in Pa s.

and slabs (LVVs, Figure 9a) and (II) without cratons and slabs but instead assuming a constant temperature of 1,375°C (Figure 9b). In the first scenario (I), due to the presence of the LVVs beneath the nominal depth of the lithospheric base, the patterns of predicted plate motions with different uniform lithosphere thicknesses are quite similar to the patterns with variable lithospheric thickness in most regions, since the basal tractions due to mantle flow are not significantly altered (Conrad & Lithgow-Bertelloni, 2006). This is especially evident when we compare the angular misfit from model predictions with variable lithosphere thickness (Figures 6c) to predictions with different uniform lithosphere thicknesses (Figures 9a, second line) showing a similar minimum at friction coefficients 0.02 for LVV cutoff $\eta = 10^{20}$ Pas. However, in models with constant temperature in the asthenosphere, we have obtained larger angular misfits, even with RMS similar to those in Figure 9a. This suggests that the presence of cratons and potentially slabs is necessary to correctly predict the plate motion orientations. In summary, thinner lithospheric plates (60 km and 80 km) are moving relatively fast with the largest rms velocities $\sim$ 13 cm/yr and $\sim$ 11 cm/yr respectively, compared to a thicker lithosphere (100 km and 150 km) with the largest rms velocities of $\sim$ 9 cm/yr and $\sim$ 8 cm/yr, respectively. As we increase the strength of the plate boundaries, all rms estimates for the predicted plate velocities decrease monotonically to $\sim$ 1 cm/yr or less, as in the case of the models using variable lithosphere thickness.

On average we obtain faster plate velocities using lithosphere thicknesses 60 km and 80 km than for the variable lithosphere thickness, whereas simulations with thicknesses 100 km and 150 km lead to a relatively lower speed with or without the effect of cratons and slabs. Significantly higher plate velocities of the thin lithospheric plates (60 km and 80 km) are due to thicker asthenosphere, that decreases the internal mantle traction by almost one third (Conrad & Lithgow-Bertelloni, 2006; Stoddard & Abbott, 1996), resulting in a lower resistance from the viscous/mantle drag to the slab pull or mantle suction forces. On the other hand, velocities with the thicker lithosphere plates are slower, because the internal mantle drag force through the thin asthenospheric layer at the base of the lithosphere provides more resistance to the driving force (Conrad & Lithgow-Bertelloni, 2006; van Summeren et al., 2012). The thinner the asthenospheric layer is the stronger is the driving force required to match observations. van Summeren et al. (2012) showed that, with no asthenosphere (i.e. using the reference mantle viscosity value in the asthenosphere) 100% of slab pull is required to match the observed plate velocity. Among the four simulations using uniform lithospheric thickness, the one using a thickness of 100 km yields the results most comparable with our simulations using a variable thickness of the lithosphere plates. Both were able to approximately match the observed plate motions from NUVEL-1A, with similar settings of the asthenosphere viscosity cutoff and plate boundary friction giving rms of 3.58 cm/yr for a variable lithosphere thickness and 3.79 cm/yr for a uniform lithosphere thickness of 100 km.

3.6. Resulting Net Rotation

Here we estimate the excitation of net rotation (NR) of the lithosphere by the LVVs, and the influence from varying plastic yielding at the plate boundaries. We do this for different coefficients of friction at the plate boundaries and for different asthenospheric viscosity cutoffs as in the previous sections. In Figures 10 and 11, we plot the amplitudes of NR and Euler pole locations for different asthenospheric viscosity cutoff values against the strength at plate boundaries varied through the coefficient of friction, for variable and uniform lithospheric thicknesses. We have also tested how large NR can be generated with layered viscosity structure (Steinberger & Calderwood, 2006) combined with different friction coefficients at plate boundaries (Figures 10b and 10d). Theoretically, mantle buoyancy structure combined with radial/layered viscosity causes no NR, and most numerical studies have shown it to be less than 0.1% of the observed NR (e.g., Becker, 2006; Ricard et al., 1991). With the introduction of plastic yielding at the plate boundaries, however we obtain larger, but still relatively low amplitudes of NRs which are mostly $<0.1^{\circ}$/Ma.

Net rotation is close to zero when the asthenosphere viscosity is larger than 10^{20} Pas. The corresponding Euler pole locations (Figure 10c) with coefficients of friction $\mu < 0.03$ are placed in the Indian Ocean, close to most of the observation-based Euler poles, but as we increase the friction at the plate boundaries the pole location moves further away, similar to the findings of Becker (2006) who used strain-rate dependent rheology. Using layered viscosity structure tends to yield Euler poles further away from observation-based pole locations. Taken together with the low NR amplitudes, this confirms the importance of the LVVs in generating NR as previously suggested in several studies (e.g., Alisic et al., 2012; Becker & Faccenna, 2009; O'Connell et al., 1991; Ricard et al., 1991; Stadler et al., 2010; Zhong, 2001). Figure 10a shows that

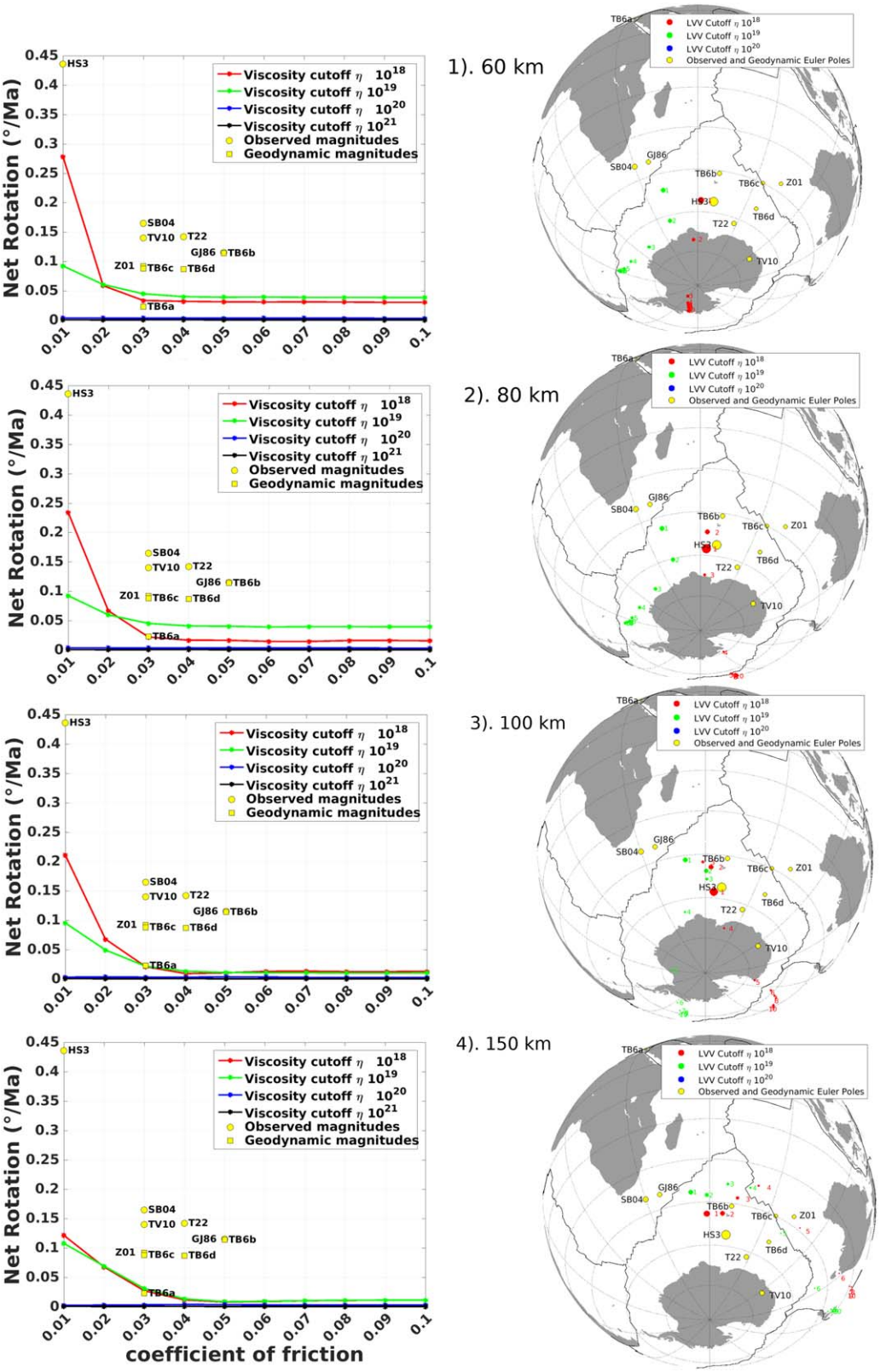

Figure 11. Net rotation amplitudes and Euler pole locations for uniform lithosphere thickness 60, 80, 100 and 150 km without the effect of cratons and slabs below each nominal depth. Numbers at colored circles in the right column, indicate the coefficient of plate boundary friction when multiplied by 0.01. Viscosity cutoff η in Pa s.

simulations with a variable lithosphere thickness and a free surface, using stress and strain-rate dependent viscosity and a 3-D thermal structure of the upper mantle are able to realistically reproduce a NR comparable to observations in a hotspot reference frame (Gordon & Jurdy, 1986; Steinberger et al., 2004; Torsvik et al., 2010; Wang & Wang, 2001) only for a low asthenosphere viscosity cutoff of $<10^{20}$ Pas. NR amplitudes constrained by azimuthal seismic anisotropy (e.g., Becker, 2008) and most of the observation-based estimates - with the exception of HS3 (Gripp & Gordon, 2002) fall within the range of 0.1 - 0.2°/Ma. Similarly, large NR amplitudes were reported by Alisic et al. (2012), who used a self-consistent global mantle flow model which also accounted for nonlinear slab rheology and plastic yielding at plate boundaries.

On the other hand, earlier 3-D numerical studies of global mantle flow (Becker, 2006; Zhong, 2001), with weak zones at plate boundaries and a free-slip top boundary condition estimated smaller NR magnitudes between 0.023 and 0.092°/Ma. This wide variation among different numerical predictions of NR amplitudes and also the deviations from observations (Čadek & Fleitout, 2003; Wen & Anderson, 1997; Zhang & Christensen, 1993) is due to different rheological models in the upper mantle and the choice of plate boundary deformation mechanism either through plastic yielding (e.g., Alisic et al., 2012; Bercovici, 1995; Tackley, 2000b) or imposed weak zones (e.g., Becker, 2006; Zhong, 2001). With larger lithosphere-asthenosphere viscosity contrast, for example with a minimum cutoff of 10^{18} Pas or 10^{19} Pas for the asthenosphere viscosity and $\mu < 0.03$ we obtain NR amplitudes that are larger than most observation-based estimates. For cutoff values below 10^{20} Pas, there is a monotonic decrease in the NR amplitudes when we increase the coefficient of friction from 0.01 to 0.1. For example, the NR amplitude will decrease from 0.365°/Ma to 0.103°/Ma if an asthenosphere viscosity cutoff of 10^{18} Pas and variable lithosphere thickness are used. A cutoff $5{\cdot}10^{19}$ Pas combined with low plate boundary friction $\mu \sim 0.03$ or less gives a net rotation which is similar to but with somewhat lower amplitudes than most of the observation-based values, and also similar to the results of Becker (2006) with temperature and strain rate dependent rheology. However, when we reduce the lithosphere-asthenosphere viscosity contrast by assigning cutoff values of 10^{20} Pas or greater, the predicted average NR amplitudes fall below 0.05°/Ma which is similar to NR in our layered viscosity model (Figure 10b) and the prediction of Becker (2006) with only strain-rate dependent rheology. A similar conclusions also follows from theoretical results (Conrad & Behn, 2010; O'Connell et al., 1991; Ricard et al., 1991) that showed that at least one order of magnitude viscosity variation is needed to excite NR comparable to observations.

The gradual decline in the NR amplitudes with increasing plate boundary friction and asthenosphere viscosity cutoff $<10^{20}$ Pas supports the idea that a significant weakening at the plate boundaries is required to initiate lithospheric net rotation (Bercovici & Richards, 2000; Zhong et al., 1998). However, the largest effect is induced by the upper mantle viscosity. This is in accord with the notion that NR of the lithosphere is largely controlled by the LVVs resulting from the sub-continental and sub-oceanic structures, mainly continental keels (Zhong, 2001), which was also supported by Becker (2006) who used a model with strain-rate and temperature-dependent LVVs, and Gérault et al. (2012) using low-viscosity plate boundaries. The 2D-cylindrical-axisymmetric study of Gérault et al. (2012) gives a convenient way to estimate the influence of slab dip angle, slab rheology and trench properties on lithosphere NR, since there is no edge toroidal flow around slabs. In 3-D geometry these additional complexities arise, and it is furthermore possible to study the effect of depth and lateral extent of continental roots. Using 3-D geometry, Becker and Faccenna (2009) found that the slab contribution to NR is lower than that of the continental keels.

Becker (2006) showed that models with strain-rate and temperature-dependent rheology yield NR amplitudes close to observations in a hotspot reference frame, while the use of only strain-rate dependent rheology resulted in an amplitude underestimation. Our resulting Euler pole locations (Figure 10c) are mainly confined to the Indian Ocean and surroundings, with the locations moving southward toward the Antarctic continent as we increase the plate boundary friction to 0.1. This robust result occurs over a broad range of asthenospheric mantle viscosity cutoff values, even those that generate smaller NR amplitudes. With friction coefficients $\mu < 0.04$ and asthenosphere viscosity cutoff of $<10^{20}$ Pas, we are able to predict Euler pole locations in the vicinity of the observed present-day NR Euler pole locations (Gordon & Jurdy, 1986; Gripp & Gordon, 2002; Steinberger et al., 2004; Wang & Wang, 2001), and those obtained from previous numerical studies (Becker, 2006; Stadler et al., 2010; Zhong, 2001).

Next, we test how the choice of a constant asthenosphere temperature (no cratons and slabs) and a constant lithospheric thickness influences the predicted net rotation. With the lowest plate boundary friction

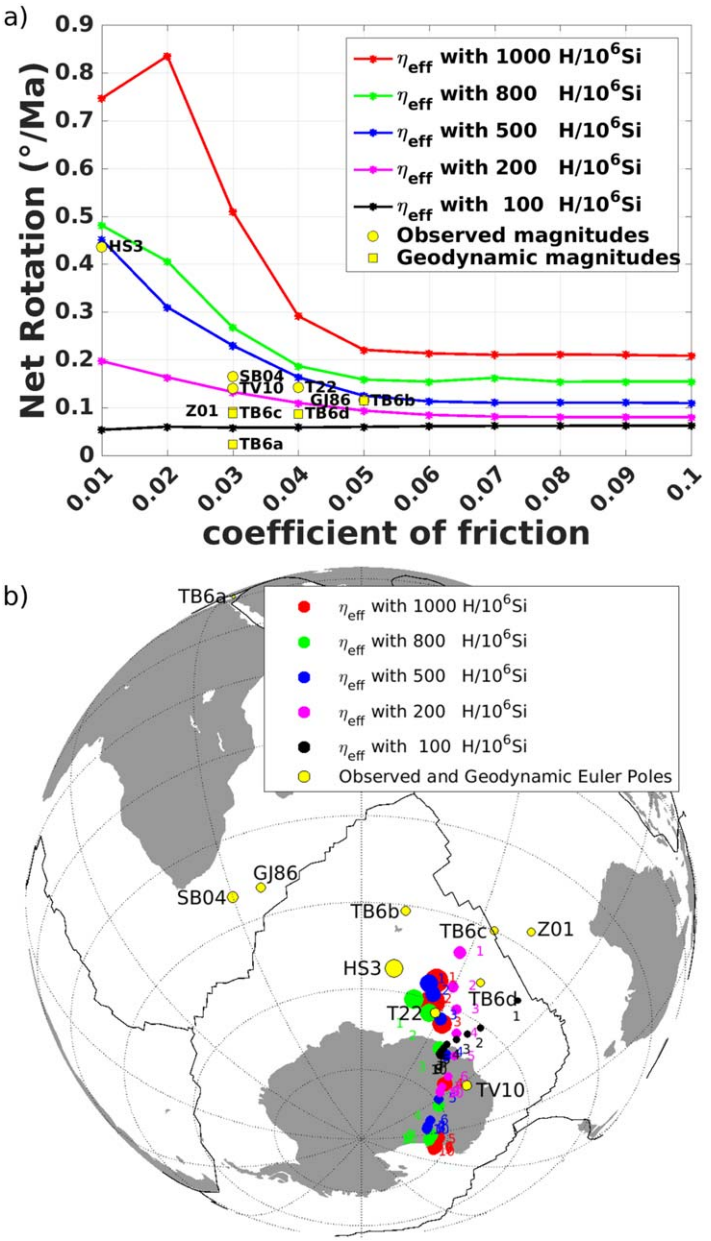

Figure 12. (a) Predicted net rotation (NR) for different water content in the asthenosphere compared with observation-based estimates and previous numerical predictions (as in Figure 10) and (b) Corresponding Euler pole locations. Numbers at colored circles in c and d indicate coefficient of plate boundary friction when multiplied by 0.01.

μ=0.01, for every uniform lithosphere thickness some net rotation is excited for low asthenosphere viscosity cutoff of 10^{18} Pas and 10^{19} Pas. For $\mu > 0.01$, and without the presence of continental keels, the predicted NR amplitude falls around or below 0.05°/Ma (Figure 11, left column), compared to higher values with cratons (see supporting information Figure S10). As an important component of the upper mantle structure continental keels are known to generate lithospheric NR (Becker, 2006; van Summeren et al., 2012; Zhong, 2001). For example, Zhong (2001) varied the thickness of the cratonic root and suggested that continental keels contribute $\sim$ 80% to lithosphere NR. This is also supported by Rudolph and Zhong (2014), who studied the influence of continental keels extending to the transition zone on NR for the past 200 Ma. However, none of our models with assumed uniform lithosphere thickness with or without cratons and slabs below the nominal lithosphere was able to predict the NR amplitude by Gripp and Gordon (2002). With the presence of continental keels in the asthenosphere, the 60 km lithosphere thickness gave about 85% of the HS3 amplitude (see supporting information Figure S10) for viscosity cutoff 10^{18} Pas with a gradual decrease, as we increase the friction coefficient, while the corresponding calculation without continental keels shows $\sim$ 60% of HS3 for $\mu = 0.01$ and suddenly falls to $\sim$ 10% of HS3 for $\mu > 0.01$ (Figure 11a). Also increasing the uniform lithosphere thickness with/without cratons and slabs beneath the nominal lithosphere gives a general decrease in the NR amplitudes for all the coefficients of friction (Figure 11 and supporting information Figure S10), with 60 km thickness tending to give larger NR than 150 km.

3.7. Water Content in the Asthenosphere

Lastly, we study how a weak asthenosphere due to high olivine water content (see section 3.1, Figure 4b and supporting information Tables S1–S5) influences the lithospheric net rotation. Here we do not apply an asthenosphere viscosity cutoff with the natural minimum viscosity in our model occurring at 10^{17} Pas. Modeled plate velocities with 1,000 H/10^{6}Si in the asthenosphere exceed $\sim$ 20 cm/yr leading to the largest net rotation amplitude of up to $\sim$ 0.8349°/Ma (Figure 12a, red profile) and giving a global rms >14 cm/yr for μ=0.01 (see supporting information Figure S11). A twofold decrease in the olivine water content (i.e. 500 H/10^{6}Si) in the asthenospheric layer above 300 km depth, resulted in lower net rotations, similar to most of the observation-based estimates of around 0.1-0.2°/Ma, even for low coefficients of plate boundary friction $\mu = 0.03$ or less. When we increase the plastic yield at plate boundaries, we observe monotonic decrease in NR amplitudes similar to our previous calculations. The Euler pole locations (Figure 12b) for different olivine water content in the asthenosphere do not deviate significantly from each other, but all show a similar southward drift for higher values of plate boundary friction.

4. Conclusions

We have studied effects of plastic yielding at plate boundaries and lateral viscosity variations (LVV) beneath lithospheric plates (due to deep cratonic roots, strong subducting slabs, and cooling of oceanic plates), on present-day plate velocities and net rotation of the lithosphere. From our results it is evident that frictional deformation at the plate boundaries influences both magnitude and orientation of plate velocities. To match the observed plate velocities in a no-net rotation reference frame, the frictional coefficient for the

plate boundary yield stress should be less than 0.04 and the asthenospheric viscosity within the range of $\sim 10^{18}-10^{20}$ Pas. To additionally match lithosphere net rotations, asthenosphere viscosity $\sim 1-5 \cdot 10^{19}$ Pas is preferred. Our inferred frictional parameters are similar to those used in previous studies to initiate and sustain subduction (Becker & Faccenna, 2009; Gerbault et al., 2009; Hall et al., 2003; Hassani et al., 1997; Sobolev & Babeyko, 2005; Tan et al., 2012). However, high values of frictional coefficient along plate boundaries lead to an almost stagnant lithospheric lid instead of moving lithosphere plates, as has also been reported by Crameri and Tackley (2015), hence lithospheric plates have strong interior (Zhong & Watts, 2013) and weak boundaries (Carena & Moder, 2009; Iaffaldano et al., 2006; Sobolev & Babeyko, 2005). We conclude that to attain the observed velocity of plate motions due to slab pull and slab suction, the inter-plate frictional force has to be low, with coefficient of friction $\mu \sim 0.02$ to 0.04. Previous geodynamic studies have imposed viscosity drop at plate boundaries (e.g., Becker, 2006) to allow the motion of the individual plates relative to each other or prescribed velocities as a boundary condition in mantle flow studies (Becker & O'Connell, 2001; Steinberger et al., 2004)

Also, plate boundary friction must be low to allow plates to obtain the observed magnitude of net rotation (NR) and Euler pole location, as high values of friction coefficient tend to cause the location of the Euler pole to drift southward to Antarctica. This was also shown with layered viscosity structure with plastic yielding at plate boundaries, which excites little to no net rotation of the lithosphere. NR amplitude is strongly influenced by viscosity in the asthenosphere and by lateral viscosity variations due to the presence of cratonic roots (Zhong, 2001). We are able to match observation-based NR amplitudes in the range of 0.1°/Ma to 0.2°/Ma and the location of the Euler pole (Doubrovine et al., 2012; Gordon & Jurdy, 1986; Steinberger et al., 2004; Torsvik et al., 2010; Wang & Wang, 2001) with $\mu < 0.05$ and asthenosphere minimum viscosity cutoff 10^{19} Pas to $5 \cdot 10^{19}$ Pas. With larger lithosphere-asthenosphere viscosity contrast of $\sim 4-5$ orders of magnitude and low friction coefficients $\mu < 0.04$ we are able to predict a larger NR amplitude in close agreement with the observations reported by Gripp and Gordon (2002) (HS3) and some results of previous numerical studies (Alisic et al., 2012; Conrad & Behn, 2010; Gérault et al., 2012; Stadler et al., 2010), while with $\mu > 0.05$ we obtain too low NR amplitudes. Our dynamically self-consistent coupled lithosphere-mantle flow model includes plastic yielding at plate boundaries, as almost all successful numerical models (Alisic et al., 2012; Stadler et al., 2010) that have been able to match observed NR amplitudes, instead of a weak zone/viscosity drop, and we treat our upper boundary as a free surface. Our preferred NR with magnitude 0.10°/Ma and Euler pole location 49.31°S and 74.88°E was obtained with a minimum viscosity cutoff of $5 \cdot 10^{19}$ Pas and $\mu = 0.02$, which also gives a plate velocity prediction that fits the observed plate motion in a NNR reference frame. Calculations with a uniform lithosphere thickness and constant temperature below each nominal lithosphere thickness (60, 80, 100 and 150 km) excite little or no NR for friction coefficients $\mu = 0.02$ or greater. Hence, we suggest that to match observed plate motion and NR with numerical models it is important to consider a combined visco-elasto-plastic rheology in the upper mantle structure (here we considered only the top 300 km), with a friction coefficient less than 0.04 at plate boundaries (plastic yielding) and minimum mantle viscosity (LVVs) cut-off of $1-5 \cdot 10^{19}$ Pas. Simulations with olivine water content 200 H/10^6Si with $\mu = 0.03$ gave an rms plate velocity of 3.90 cm/yr close to the observed rms plate velocities (DeMets et al., 2010; Torsvik et al., 2010), and also gave an NR amplitude of 0.14°/Ma with the pole location 56.62°S and 89.85°E, again close to observational-based values.

Acknowledgments
This work was funded by the Helmholtz graduate school GeoSim together with the Helmholtz Centre Potsdam-GFZ German Research Centre for Geosciences. Irina Rogozhina has been supported by the BMBF German Climate Modeling Initiative PalMod. The coupled global numerical code that was used to generate the results in this study builds on the SLIM3D (Popov & Sobolev, 2008) code and the spectral code of Hager and O'Connell (1981) and are available upon request from the corresponding authors. The rheological parameters used for the upper mantle are provided in the main and supporting information as tables. We have uploaded the 3-D temperature model, which were used in the top 300 km of the upper mantle for our calculations supporting information supporting information. Also the velocity-to-density scaling profile used to convert the Smean seismic topography (Becker & Boschi, 2002), used below the 300 km depth with the corresponding viscosity profile. Lastly, we thank the two anonymous reviewers for the constructive comments to improve our manuscript.

References

Alisic, L., Gurnis, M., Stadler, G., Burstedde, C., & Ghattas, O. (2012). Multi-scale dynamics and rheology of mantle flow with plates. *Journal of Geophysical Research*, *117*, B10402. https://doi.org/10.1029/2012JB009234

Artemieva, I. (2006). Global 1°×1° thermal model TC1 for the continental lithosphere: Implications for lithosphere secular evolution. *Tectonophysics*, *416*, 245–277.

Artemieva, I. M., & Mooney, W. D. (2002). On the relations between cratonic lithosphere thickness, plate motions, and basal drag. *Tectonophysics*, *358*(1–4), 211–231. https://doi.org/10.1016/S0040-1951(02)00425-0

Artyushkov, E. V. (1973). Stresses in the lithosphere caused by crustal thickness inhomogeneities. *Journal of Geophysical Research*, *78*, 7675–7708.

Becker, T. W. (2006). On the effect of temperature and strain-rate dependent viscosity on global mantle flow, net rotation, and plate-driving forces. *Geophysical Journal International*, *167*(2), 943–957.

Becker, T. W. (2008). Azimuthal seismic anisotropy constrains net rotation of the lithosphere. *Geophysical Research Letters*, *35*, L05303. https://doi.org/10.1029/2007GL032928

Becker, T. W., & Boschi, L. (2002). A comparison of tomographic and geodynamic mantle models. *Geochemistry, Geophysics, Geosystems*, *3*(1), 1003. https://doi.org/10.1029/2001GC000168

Becker, T. W., & Faccenna, C. (2009). A review of the role of subduction dynamics for regional and global plate motions. In F. Funiciello & S. Lallemand (Eds.), *Subduction zone geodynamics* (Int. J. Earth Sci., pp. 3–34). Berlin Heidelberg: Springer-Verlag.

Becker, T. W., & O'Connell, R. J. (2001). Predicting plate velocities with geodynamic models. *Geochemistry, Geophysics, Geosystems*, *2*(12), 1060. https://doi.org/10.1029/2001GC000171

Becker, T. W., Schaeffer, A. J., Lebedev, S., & Conrad, S. P. (2015). Toward a generalized plate motion reference frame. *Geophysical Research Letters*, *42*, 3188–3196. https://doi.org/10.1002/2015GL063695

Bercovici, D. (1995). A source-sink model of the generation of plate-tectonics from non-Newtonian mantle flow. *Journal of Geophysical Research*, *100*, 2013–2030.

Bercovici, Y., Ricard, D., & Richards, M. A. (2000). The relation between mantle dynamics and plate tectonics: A primer. In M. A. Richards, R. G. Gordon & R. D. Van Der Hilst (Eds.), *The history and dynamics of global plate motions* (Geophysical Monograph Vol. 121, pp. 5–46). Washington, DC: American Geophysical Union. https://doi.org/10.1029/GM121p0005

Bird, P. (1989). New finite element techniques for modeling deformation histories of continents with stratified temperature-dependent rheology. *Journal of Geophysical Research*, *94*, 3967–3990. https://doi.org/10.1029/JB094iB04p03967

Bird, P. (2003). An updated digital model of plate boundaries. *Geochemistry, Geophysics, Geosystems*, *4*(3), 1027. https://doi.org/10.1029/2001GC000252

Bird, P., & Kong, X. (1994). Computer simulations of California tectonics confirm very low strength of major faults. *GSA Bulletin*, *106*(2), 159–174. https://doi.org/10.1130/0016-7606(1994)106<0159:CSOCTC>2.3.CO;2

Bird, P., Liu, Z., & Rucker, W. K. (2008). Stresses that drive the plates from below: Definitions, computational path, model optimization, and error analysis. *Journal of Geophysical Research*, *113*, B11406. https://doi.org/10.1029/2007JB005460

Brune, S., Heine, C., Pérez-Gussinyé, M., & Sobolev, S. V. (2014). Rift migration explains continental margin asymmetry and crustal hyper-extension. *Nature Communications*, *5*, 4014. https://doi.org/10.1038/ncomms5014

Brune, S., Popov, A. A., & Sobolev, S. V. (2012). Modeling suggests that oblique extension facilitates rifting and continental break-up. *Journal of Geophysical Research*, *117*, B08402. https://doi.org/10.1029/2011JB008860

Brune, S., Williams, S. E., Butterworth, N. P., & Müller, R. D. (2016). Abrupt plate accelerations shape rifted continental margins. *Nature*, *536*(7615), 201–204. https://doi.org/10.1038/nature18319

Burov, E. B. (2011). Rheology and strength of the lithosphere. *Marine and Petroleum Geology*, *28*(8), 1402–1443.

Byerlee, J. (1978). Friction of rock. *Pure and Applied Geophysics*, *116*, 615–626.

Čadek, O., & Fleitout, L. (2003). Effect of lateral viscosity variations in the top 300 km of the mantle on the geoid and dynamic topography. *Geophysical Journal International*, *152*, 566–580.

Carena, S., & Moder, C. (2009). The strength of faults in the crust in the western United States. *Earth and Planetary Science Letters*, *287*(3–4), 373–384. https://doi.org/10.1016/j.epsl.2009.08.021

Carlson, R. W., Pearson, D. G., & James, D. E. (2005). Physical, chemical, and chronological characteristics of continental mantle. *Reviews of Geophysics*, *43*, RG1001. https://doi.org/10.1029/2004RG000156

Cerpa, N. G., Hassani, R., Gerbault, M., & Prévost, J.-H. (2014). A fictitious domain method for lithosphere-asthenosphere interaction: Application to periodic slab folding in the upper mantle. *Geochemistry, Geophysics, Geosystems*, *15*, 1852–1877. https://doi.org/10.1002/2014GC005241

Conrad, C. P., & Behn, M. (2010). Constraints on lithosphere net rotation and asthenospheric viscosity from global mantle flow models and seismic anisotropy. *Geochemistry, Geophysics, Geosystems*, *11*, Q05W05. https://doi.org/10.1029/2009GC002970

Conrad, C. P., & Lithgow-Bertelloni, C. (2002). How mantle slabs drive plate tectonics. *Science*, *298*(5591), 207–209.

Conrad, C. P., & Lithgow-Bertelloni, C. (2004). The temporal evolution of plate driving forces: Importance of "slab suction" versus "slab pull" during the Cenozoic. *Journal of Geophysical Research*, *109*, B10407. https://doi.org/10.1029/2004JB002991

Conrad, C. P., & Lithgow-Bertelloni, C. (2006). Influence of continental roots and asthenosphere on plate-mantle coupling. *Geophysical Research Letters*, *33*, L05312. https://doi.org/10.1029/2005GL025621

Crameri, F., & Tackley, P. J. (2014). Spontaneous development of arcuate single-sided subduction in global 3-d mantle convection models with a free surface. *Journal of Geophysical Research: Solid Earth*, *119*, 5921–5942. https://doi.org/10.1002/2014JB010939

Crameri, F., & Tackley, P. J. (2015). Parameters controlling dynamically self-consistent plate tectonics and single-sided subduction in global models of mantle convection. *Journal of Geophysical Research: Solid Earth*, *120*, 3680–3706. https://doi.org/10.1002/2014JB011664

Danyushevsky, L. V., Eggins, S. M., Falloon, T. J., & Christie, D. M. (2000). H_2O abundance in depleted to moderately enriched mid-ocean ridge magmas; part I: Incompatible behaviour, implications for mantle storage, and origin of regional variations. *Journal of Petrology*, *41*(8), 1329–1364. https://doi.org/10.1093/petrology/41.8.1329

Davies, G. F. (1978). The roles of boundary friction, basal shear stress and deep mantle convection in plate tectonics. *Geophysical Research Letters*, *5*, 161–164. https://doi.org/10.1029/GL005i003p00161

DeMets, C., Gordon, R. G., & Argus, D. F. (2010). Geologically current plate motions. *Geophysical Journal International*, *181*(1), 1–80.

Doubrovine, P. V., Steinberger, B., & Torsvik, T. H. (2012). Absolute plate motions in a reference frame defined by moving hot spots in the Pacific, Atlantic, and Indian oceans. *Journal of Geophysical Research*, *117*, B09101. https://doi.org/10.1029/2011JB009072

Dziewonski, A. M., & Anderson, D. L. (1981). Preliminary reference Earth model. *Physics of the Earth and Planetary Interiors*, *25*(4), 297– 356. https://doi.org/10.1016/0031-9201(81)90046-7

Faccenda, M., Gerya, T. V., & Burlini, L. (2009). Deep slab hydration induced by bending-related variations in tectonic pressure. *Nature Geoscience*, *2*(11), 790–793. https://doi.org/10.1038/ngeo656

Faccenna, C., Heuret, A., Funiciello, F., Lallemand, S., & Becker, T. W. (2007). Predicting trench and plate motion from the dynamics of a strong slab. *Earth and Planetary Science Letters*, *257*(1–2), 29–36.

Fischer, K. M., Ford, D. L., Abt, H. A., & Rychert, C. A. (2010). The lithosphere-asthenosphere boundary. *Annual Review of Earth and Planetary Sciences*, *38*(1), 551–575.

Forsyth, D. W., & Uyeda, S. (1975). On the relative importance of the driving forces of plate motion. *Geophysical Journal of Royal Astronomical Society*, *43*(1), 163–200.

Gao, X., & Wang, K. (2014). Strength of stick-slip and creeping subduction megathrusts from heat flow observations. *Science*, *345*(6200), 1038–1041. https://doi.org/10.1126/science.1255487

Gérault, M., Becker, T. W., Kaus, B. J. P., Faccenna, C., Moresi, L. N., & Husson, L. (2012). The role of slabs and oceanic plate geometry for the net rotation of the lithosphere, trench motions, and slab return flow. *Geochemistry, Geophysics, Geosystems*, *13*, Q04001. https://doi.org/10.1029/2011GC003934

Gerbault, M., Cembrano, J., Mpodozis, C., Farias, M., & Pardo, M. (2009). Continental margin deformation along the Andean subduction zone: Thermo-mechanical models. *Physics of the Earth and Planetary Interiors*, *177*(3–4), 180–205. https://doi.org/10.1016/j.pepi.2009.09.001

Ghosh, A., & Holt, W. E. (2012). Plate motions and stresses from global dynamic models. *Science*, *335*(6070), 838–843.

Gordon, R. G., & Jurdy, D. M. (1986). Cenozoic global plate motions. *Journal of Geophysical Research*, *91*, 12389–12406.

Green, D. H., Hibberson, W. O., Kovacs, I., & Rosenthal, A. (2010). Water and its influence on the lithosphere-asthenosphere boundary. *Nature*, *467*(7314), 448–451. https://doi.org/10.1038/nature09369

Griffin, W. L., O'Reilly, S. Y., Doyle, B. J., Pearson, N. J., Coopersmith, H., Kivi, K., et al. (2004). Lithosphere mapping beneath the North American plate. *Lithos*, *77*(1–4), 873–922. https://doi.org/10.1016/j.lithos.2004.03.034

Gripp, A. E., & Gordon, R. G. (2002). Young tracks of hotspots and current plate velocities. *Geophysical Journal International*, *150*(2), 321–361.

Gung, Y., Panning, M., & Romanowicz, B. (2003). Global anisotropy and the thickness of continents. *Nature*, *422*, 707–711. https://doi.org/10.1038/nature01559

Gurnis, M., Hall, C., & Lavier, L. (2004). Evolving force balance during incipient subduction. *Geochemistry, Geophysics, Geosystems*, *5*, Q07001. https://doi.org/10.1029/2003GC000681

Hager, B. H., & O'Connell, R. J. (1979). Kinematic models of large-scale flow in the Earth's mantle. *Journal of Geophysical Research*, *84*, 1031–1048.

Hager, B. H., & O'Connell, R. J. (1981). A simple global model of plate dynamics and mantle convection. *Journal of Geophysical Research*, *86*, 4843–4867.

Hall, C. E., Gurnis, M., Sdrolias, M., Lavier, L. L., & Müller, R. D. (2003). Catastrophic initiation of subduction following forced convergence at transform boundaries. *Earth and Planetary Science Letters*, *212*(1–2), 15–30.

Harper, J. F. (1975). On the driving forces of plate tectonics. *Geophysical Journal of Royal Astronomical Society*, *40*, 465–474.

Hassani, R., Jongmans, D., & Chéry, J. (1997). Study of plate deformation and stress in subduction processes using two-dimensional numerical models. *Journal of Geophysical Research*, *102*, 17951–17965.

Hirth, G., & Kohlstedt, D. L. (1996). Water in the oceanic upper mantle: Implications for rheology, melt extraction and the evolution of the lithosphere. *Earth and Planetary Science Letters*, *144*(1–2), 93– 108. https://doi.org/10.1016/0012-821X(96)00154-9

Hirth, G., & Kohlstedt, D. L. (2004). Rheology of the upper mantle and the mantle wedge: A view from the experimentalists. In J. Eiler (Ed.), *Inside the subduction factory* (Geophys. Monograph, Vol. 138, pp. 83–105). Washington, DC: American Geophysical Union.

Humphreys, E. D., & Coblentz, D. D. (2007). North American dynamics and western U.S. tectonics. *Reviews of Geophysics*, *45*, RG3001. https://doi.org/10.1029/2005RG000181

Iaffaldano, G., Bunge, H.-P., & Dixon, T. H. (2006). Feedback between mountain belt growth and plate convergence. *Geology*, *34*(10), 893–896. https://doi.org/10.1130/G22661.1

Kameyama, M., Yuen, D. A., & Karato, S. (1999). Thermal-mechanical effects of low-temperature plasticity (the Peierls mechanism) on the deformation of a viscoelastic shear zone. *Earth and Planetary Science Letters*, *168*(1–2), 159–172. https://doi.org/10.1016/S0012-821X(99)00040-0

Karato, S. (2010). Rheology of the deep upper mantle and its implications for the preservation of the continental roots: A review. *Tectonophysics*, *481*(1–4), 82–98.

Karato, S., & Wu, P. (1993). Rheology of the upper mantle: A synthesis. *Science*, *260*(5109), 771–778.

Karato, S-I. (2012). On the origin of the asthenosphere. *Earth and Planetary Science Letters*, *321–322*, 95–103.

Kaus, B. J. P., Steedman, C., & Becker, T. W. (2008). From passive continental margin to mountain belt: Insights from analytical and numerical models and application to Taiwan. *Physics of the Earth and Planetary Interiors*, *171*(1–4), 235–251.

Kawakatsu, H., Kumar, P., Takei, Y., Shinohara, M., Kanazawa, T., Araki, E., & Suyehiro, K. (2009). Seismic evidence for sharp lithosphere-asthenosphere boundaries of oceanic plates. *Science*, *324*(5926), 499–502.

Lamb, S., & Davis, P. (2003). Cenozoic climate change as a possible cause for the rise of the Andes. *Nature*, *425*(6960), 792–797. https://doi.org/10.1038/nature02049

Lithgow-Bertelloni, C., & Richards, M. A. (1995). Cenozoic plate driving forces. *Geophysical Research Letters*, *22*, 1317–1320.

Lithgow-Bertelloni, C., & Richards, M. A. (1998). The dynamics of Cenozoic and Mesozoic plate motions. *Review of Geophysics*, *36*, 27–78.

Lithgow-Bertelloni, C., & Silver, P. G. (1998). Dynamic topography, plate driving forces and the African superswell. *Nature*, *395*(6699), 269–272.

McKenzie, D. P. (1972). Plate tectonics. In E. C. Robertson (Ed.), *The nature of the solid earth* (pp. 323–360). New York, NY: McGraw-Hill.

Michael, P. (1995). Regionally distinctive sources of depleted MORB: Evidence from trace elements and H_2O. *Earth and Planetary Science Letters*, *131*(3), 301–320. https://doi.org/10.1016/0012-821X(95)00023-6

Minster, J. B., Jordan, T. H., Molnar, P., & Haines, E. (1974). Numerical modelling of instantaneous plate tectonics. *Geophysical Journal of Royal Astronomical Society*, *36*(3), 541–576. https://doi.org/10.1111/j.1365-246X.1974.tb00613.x

Mitrovica, J. X. (1996). Haskell [1935] revisited. *Journal of Geophysical Research*, *101*, 555–569. https://doi.org/10.1029/95JB03208

Mitrovica, J. X., & Forte, A. M. (1997). Radial profile of mantle viscosity: Results from the joint inversion of convection and postglacial rebound observables. *Journal of Geophysical Research*, *102*, 2751–2769. https://doi.org/10.1029/96JB03175

Moresi, L., Gurnis, M., & Zhong, S. (2000). Plate tectonics and convection in the Earth's mantle: Toward a numerical simulation. *Computing in Science and Engineering*, *2*, 22–33. https://doi.org/10.1109/5992.841793

Moresi, L. N., & Solomatov, V. (1998). Mantle convection with a brittle lithosphere: Thoughts on the global tectonic styles of the Earth and Venus. *Geophysical Journal International*, *133*(3), 669–682.

Mount, V. S., & Suppe, J. (1987). State of stress near the San Andreas fault: Implications for wrench tectonics. *Geology*, *15*(12), 1143–1146. https://doi.org/10.1130/0091-7613(1987)15<1143:SOSNTS>2.0.CO;2

Müller, R. D., Sdrolias, M., Gaina, C., & Roest, W. R. (2008). Age, spreading rates and spreading asymmetry of the world's ocean crust. *Geochemistry, Geophysics, Geosystems*, *9*, Q04006. https://doi.org/10.1029/2007GC001743

Nesbitt, H. W., & Young, G. M. (1982). Early Proterozoic climates and plate motions inferred from major element chemistry of lutites. *Nature*, *299*(5885), 715–717. https://doi.org/10.1038/299715a0

O'Connell, R. J., Gable, C. W., & Hager, B. H. (1991). Toroidal-poloidal partitioning of lithospheric plate motions. In R. Sabadini & K. Lambeck (Eds.), *Glacial isostasy, Sea-level and mantle rheology* (pp. 535–551). Norwell, MA: Kluwer Academic Publishers.

Oleskevich, D. A., Hyndman, R. D., & Wang, K. (1999). The updip and downdip limits to great subduction earthquakes: Thermal and structural models of Cascadia, South Alaska, SW Japan, and Chile. *Journal of Geophysical Research*, *104*, 14965–14991. https://doi.org/10.1029/1999JB900060

Osei Tutu, A., Steinberger, B., Sobolev, S. V., Rogozhina, I., & Popov, A. A. (2017). Effects of upper mantle heterogeneities on lithospheric stress field and dynamic topography. *Solid Earth Discussions*, 2017. https://doi.org/10.5194/se-2017-111

Popov, A., & Sobolev, S. V. (2008). SLIM3D: A tool for three-dimensional thermomechanical modeling of lithospheric deformation with elasto-visco-plastic rheology. *Physics of the Earth and Planetary Interiors*, *171*(1–4), 55–75. https://doi.org/10.1016/j.pepi.2008.03.007

Quinteros, J., & Sobolev, S. V. (2013). Why has the Nazca plate slowed since the Neogene? *Geology*, *41*(1), 31–34.

Raymo, M. E., & Ruddiman, W. F. (1992). Tectonic forcing of late cenozoic climate. *Nature*, *359*(6391), 117–122. https://doi.org/10.1038/299715a0

Ricard, Y., Doglioni, C., & Sabadini, R. (1991). Differential rotation between lithosphere and mantle: A consequence of lateral mantle viscosity variations. *Journal of Geophysical Research*, *96*, 8407–8415.

Richards, M., Yang, W.-S., Baumgardner, J., & Bunge, H.-P. (2001). Role of a low-viscosity zone in stabilizing plate tectonics: Implications for comparative terrestrial planetology. *Geochemistry, Geophysics, Geosystems*, *2*(8), 1026. https://doi.org/10.1029/2000GC000115

Reigber, C., Schmidt, R., Flechtner, F., König, R., Meyer, U., Neumayer, K., et al. (2005). An Earth gravity field model complete to degree and order 150 from GRACE: EIGEN-GRACE02S. *Journal of Geodynamics*, *39*(1), 1–10. https://doi.org/10.1016/j.jog.2004.07.001

Rudolph, M. L., & Zhong, S. J. (2014). History and dynamics of net rotation of the mantle and lithosphere. *Geochemistry, Geophysics, Geosystems*, *15*, 3645–3657. https://doi.org/10.1002/2014GC005457

Rychert, K. A., Fischer, K. M., & Rondenay, S. (2005). A sharp lithosphere-asthenosphere boundary imaged beneath eastern North America. *Nature*, *436*(7050), 542–545.

Schaeffer, A., & Lebedev, S. (2013). Global shear speed structure of the upper mantle and transition zone. *Geophysical Journal International*, *194*(1), 417–449.

Schellart, W. P. (2004). Kinematics of subduction and subduction-induced flow in the upper mantle. *Journal of Geophysical Research*, *109*, B07401. https://doi.org/10.1029/2004JB002970

Schlaphorst, D., Kendall, J.-M., Collier, J. S., Verdon, J. P., Blundy, J., Baptie, B., et al. (2016). Water, oceanic fracture zones and the lubrication of subducting plate boundaries insights from seismicity. *Geophysical Journal International*, *204*(3), 1405–1420. https://doi.org/10.1093/gji/ggv509

Schmerr, N. (2012). The Gutenberg discontinuity: Melt at the lithosphere-asthenosphere boundary. *Science*, *335*(6075), 1480–1483. https://doi.org/10.1126/science.1215433

Schwartz, S. Y., & Rokosky, J. M. (2007). Slow slip events and seismic tremor at circum-Pacific subduction zones. *Reviews of Geophysics*, *45*, RG3004. https://doi.org/10.1029/2006RG000208

Sobolev, A. V., & Chaussidon, M. (1996). Concentrations in primary melts from supra-subduction zones and mid-ocean ridges: Implications for H_2O storage and recycling in the mantle. *Earth and Planetary Science Letters*, *137*(1–4), 45–55. https://doi.org/10.1016/0012-821X(95)00203-O

Sobolev, S. V., & Babeyko, A. Y. (2005). What drives orogeny in the Andes? *Geology*, *33*(8), 617–620.

Sobolev, S. V., Babeyko, A. Y., Koulakov, I., & Oncken, O. (2006). Mechanism of the Andean Orogeny: Insight from numerical modeling. In O Oncken et al. (Eds.), *The Andes, Frontiers in Earth Sciences Book Series* (pp. 513–535). Berlin, Germany: Springer. https://doi.org/10.1007/978-3-540-48684-8_25

Sobolev, S. V., Popov, A., & Steinberger, B. (2009). Constraining rheology and water content in the upper mantle by modeling plate tectonics. *Geochimica et Cosmochimica Acta*, *73*, A1244.

Stadler, G., Gurnis, M., Burstedde, C., Wilcox, L. C., Alisic, L., & Ghattas, O. (2010). The dynamics of plate tectonics and mantle flow: From local to global scales. *Science*, *329*(5995), 1033–1038.

Steinberger, B. (2000). Slabs in the lower mantle – results of dynamic modelling compared with tomographic images and the geoid. *Physics of the Earth and Planetary Interiors*, *118*, 241–257.

Steinberger, B., & Calderwood, A. (2006). Models of large-scale viscous flow in the Earth's mantle with constraints from mineral physics and surface observations. *Geophysical Journal International*, *167*(3), 1461–1481.

Steinberger, B., Schmeling, H., & Marquart, G. (2001). Large-scale lithospheric stress field and topography induced by global mantle circulation. *Earth and Planetary Science Letters*, *186*(1), 75–91.

Steinberger, B., Sutherland, R., & O'Connell, R. J. (2004). Prediction of Emperor-Hawaii seamount locations from a revised model of global plate motion and mantle flow. *Nature*, *430*(6996), 167–173.

Stoddard, P. R., & Abbott, D. (1996). Influence of the tectosphere upon plate motion. *Journal of Geophysical Research*, *101*, 5425–5433. https://doi.org/10.1029/95JB03540

Tackley, P. J. (2000a). Self-consistent generation of tectonic plates in time-dependent, three-dimensional mantle convection simulations 1. Pseudoplastic yielding. *Geochemistry, Geophysics, Geosystems*, *1(8)*, 1021, https://doi.org/10.1029/2000GC000036

Tackley, P. J. (2000b). Self-consistent generation of tectonic plates in time-dependent, three-dimensional mantle convection simulations 2. Strain weakening and asthenosphere. *Geochemistry, Geophysics, Geosystems*, *1(8)*, 1026, https://doi.org/10.1029/2000GC000043

Tan, E., Lavier, L. L., Van Avendonk, H. J. A., & Heuret, A. (2012). The role of frictional strength on plate coupling at the subduction interface. *Geochemistry, Geophysics, Geosystems*, *13*, Q10006. https://doi.org/10.1029/2012GC004214

Torsvik, T. H., Steinberger, B., Gurnis, M., & Gaina, C. (2010). Plate tectonics and net lithosphere rotation over the past 150 My. *Earth and Planetary Science Letters*, *291*(1–4), 106–112. https://doi.org/10.1016/j.epsl.2009.12.055.

Townend, J., & Zoback, M. D. (2004). Regional tectonic stress near the San Andreas fault in central and southern California. *Geophysical Research Letters*, *31*, L15S11. https://doi.org/10.1029/2003GL018918

Turcotte, D. L., & Oxburgh, E. R. (1967). Finite amplitude convective cells and continental drift. *Journal of Fluid Mechanics*, *28*(01), 29–42.

van Summeren, J., Conrad, C. P., & Lithgow-Bertelloni, C. (2012). The importance of slab pull and a global asthenosphere to plate motions. *Geochemistry, Geophysics, Geosystems*, *13*, Q0AK03. https://doi.org/10.1029/2011GC003873

Veevers, J. J. (1990). Tectonic-climatic supercycle in the billion-year plate-tectonic eon: Permian Pangean icehouse alternates with Cretaceous dispersed-continents greenhouse. *Sedimentary Geology*, *68*(1–2), 1–16.

von Huene, R., & Ranero, C. R. (2003). Subduction erosion and basal friction along the sediment-starved convergent margin off Antofagasta, Chile. *Journal of Geophysical Research*, *108*(B2), 2079. https://doi.org/10.1029/2001JB001569

Wang, S., & Wang, R. (2001). Current plate velocities relative to hotspots: Implications for hotspot motion, mantle viscosity and global reference frame. *Earth and Planetary Science Letters*, *189*(3–4), 133–140.

Wen, L., & Anderson, D. L. (1997). Present-day plate motion constraint on mantle rheology and convection. *Journal of Geophysical Research*, *102*, 24639–24653.

Wilks, N. L., & Carter, K. R. (1990). Rheology of some continental lower crustal rocks. *Tectonophysics*, *182*(1–2), 57–77.

Wu, B., Conrad, C. P., Heuret, A., Lithgow-Bertelloni, C., & Lallemand, S. (2008). Reconciling strong slab pull and weak plate bending: The plate motion constraint on the strength of mantle slabs. *Earth and Planetary Science Letters*, *272*(1–2), 412–421.

Yuan, H., & Romanowicz, B. (2010). Lithospheric layering in the North American craton. *Nature*, *466*, 1063–1068. https://doi.org/10.1038/nature09332

Zhang, S., & Christensen, U. (1993). Some effects of lateral viscosity variations on geoid and surface velocities induced by density anomalies in the mantle. *Geophysical Journal International*, *114*(3), 531–547.

Zhong, S. (2001). Role of ocean-continent contrast and continental keels on plate motion, net rotation of lithosphere, and the geoid. *Journal of Geophysical Research*, *106*, 703–712.

Zhong, S., & Gurnis, M. (1995). Towards a realistic simulation of plate margins in mantle convection. *Geophysical Research Letters*, *22*, 981–984.

Zhong, S., & Gurnis, M. (1996). Interaction of weak faults and non-Newtonian rheology produces plate tectonics in a 3D model of mantle flow. *Nature*, *383*(6597), 245–247.

Zhong, S., Gurnis, M., & Moresi, L. (1998). Role of faults, nonlinear rheology, and viscosity structure in generating plates from instantaneous mantle flow models. *Journal of Geophysical Research*, *103*, 15255–15268.

Zhong, S., & Watts, A. B. (2013). Lithospheric deformation induced by loading of the Hawaiian islands and its implications for mantle rheology. *Journal of Geophysical Research: Solid Earth*, *118*, 6025–6048. https://doi.org/10.1002/2013JB010408

Zhong, S., Zuber, M. T., Moresi, L., & Gurnis, M. (2000). Role of temperature-dependent viscosity and surface plates in spherical shell models of mantle convection. *Journal of Geophysical Research*, *105*, 11063–11082.

Zoback, M. D., Zoback, M. L., Mount, V. S., Suppe, J., Eaton, J. P., Healy, J. H., et al. (1987). New evidence on the state of stress of the San Andreas fault system. *Science*, *238*(4830), 1105–1111.

Zoback, M. L. (1992). First- and second-order patterns of stress in the lithosphere: The World Stress Map project. *Journal of Geophysical Research*, *97*, 11703–11728.

Zoback, M. L., Zoback, M. D., Adams, J., Assumpção, M., Bell, S., Bergman, E. A., et al. (1989). Global patterns of tectonic stress. *Nature*, *341*(6240), 291–298. https://doi.org/10.1038/341291a0